# OPTIMIZING AND QUANTIFYING $CO_2$ STORAGE RESOURCE IN SALINE FORMATIONS AND HYDROCARBON RESERVOIRS

## Final Report

*Prepared for:*

AAD Document Control

National Energy Technology Laboratory
U.S. Department of Energy
626 Cochrans Mill Road
PO Box 10940, MS 921-107
Pittsburgh, PA 15236-0940

Project Start Date: October 1, 2012
Project End Date: June 30, 2017
Cooperative Agreement No. DE-FE0009114

*Prepared by:*

Nicholas W. Bosshart
Scott C. Ayash
Nicholas A. Azzolina
Wesley D. Peck
Charles D. Gorecki
Jun Ge
Tao Jiang
Matthew E. Burton-Kelly
Parker W. Anderson
Neil W. Dotzenrod
Andrew J. Gorz

Energy & Environmental Research Center
University of North Dakota
15 North 23rd Street, Stop 9018
Grand Forks, ND 58202-9018

2017-EERC-06-18 June 2017

## EERC DISCLAIMER

LEGAL NOTICE This research report was prepared by the Energy & Environmental Research Center (EERC), an agency of the University of North Dakota, as an account of work sponsored by the U.S. Department of Energy (DOE) National Energy Technology Laboratory (NETL). Because of the research nature of the work performed, neither the EERC nor any of its employees makes any warranty, express or implied, or assumes any legal liability or responsibility for the accuracy, completeness, or usefulness of any information, apparatus, product, or process disclosed or represents that its use would not infringe privately owned rights. Reference herein to any specific commercial product, process, or service by trade name, trademark, manufacturer, or otherwise does not necessarily constitute or imply its endorsement or recommendation by the EERC.

## ACKNOWLEDGMENTS

This work was performed under the DOE NETL Cooperative Agreement No. DE-FE0009114.

The EERC is grateful for the contributions of Dr. Stefan Bachu and Mr. L. Stephen Melzer to this work. The EERC would also like to thank project partners Schlumberger Carbon Services and Computer Modelling Group for their support.

## DOE DISCLAIMER

This report was prepared as an account of work sponsored by an agency of the United States Government. Neither the United States Government, nor any agency thereof, nor any of their employees, makes any warranty, express or implied, or assumes any legal liability or responsibility for the accuracy, completeness, or usefulness of any information, apparatus, product, or process disclosed, or represents that its use would not infringe privately owned rights. Reference herein to any specific commercial product, process, or service by trade name, trademark, manufacturer, or otherwise does not necessarily constitute or imply its endorsement, recommendation, or favoring by the United States Government or any agency thereof. The views and opinions of authors expressed herein do not necessarily state or reflect those of the United States Government or any agency thereof.

# OPTIMIZING AND QUANTIFYING $CO_2$ STORAGE RESOURCE IN SALINE FORMATIONS AND HYDROCARBON RESERVOIRS

## ABSTRACT

In an effort to reduce carbon dioxide ($CO_2$) emissions from large stationary sources, carbon capture and storage (CCS) is being investigated as one approach. This work assesses $CO_2$ storage resource estimation methods for deep saline formations (DSFs) and hydrocarbon reservoirs undergoing $CO_2$ enhanced oil recovery (EOR). Project activities were conducted using geologic modeling and simulation to investigate $CO_2$ storage efficiency.

$CO_2$ storage rates and efficiencies in DSFs classified by interpreted depositional environment were evaluated at the regional scale over a 100-year time frame. A focus was placed on developing results applicable to future widespread commercial-scale $CO_2$ storage operations in which an array of injection wells may be used to optimize storage in saline formations. The results of this work suggest future investigations of prospective storage resource in closed or semiclosed formations need not have a detailed understanding of the depositional environment of the reservoir to generate meaningful estimates. However, the results of this work also illustrate the relative importance of depositional environment, formation depth, structural geometry, and boundary conditions on the *rate* of $CO_2$ storage in these types of systems.

$CO_2$ EOR occupies an important place in the realm of geologic storage of $CO_2$, as it is likely to be the primary means of geologic $CO_2$ storage during the early stages of commercial implementation, given the lack of a national policy and the viability of the current business case. This work estimates $CO_2$ storage efficiency factors using a unique industry database of $CO_2$ EOR sites and 18 different reservoir simulation models capturing fluvial clastic and shallow shelf carbonate depositional environments for reservoir depths of 1219 and 2438 meters (4000 and 8000 feet) and 7.6-, 20-, and 64-meter (25-, 66,- and 209-foot) pay zones. The results of this work provide practical information that can be used to quantify $CO_2$ storage resource estimates in oil reservoirs during $CO_2$ EOR operations (as opposed to storage following depletion) and the uncertainty associated with those estimates.

## TABLE OF CONTENTS

# LIST OF FIGURES

# LIST OF TABLES

# OPTIMIZING AND QUANTIFYING $CO_2$ STORAGE RESOURCE IN SALINE FORMATIONS AND HYDROCARBON RESERVOIRS

## EXECUTIVE SUMMARY

This report describes the scope of work, methods, results, and conclusions of a multiyear project investigating carbon dioxide ($CO_2$) storage resource assessments in geologic formations through modeling and simulation of deep saline formations (DSFs) and hydrocarbon reservoirs in association with $CO_2$ enhanced oil recovery ($CO_2$ EOR).

This project report addresses Area of Interest 3 of U.S. Department of Energy (DOE) Funding Opportunity Announcement (FOA) DE-FOA-0000652, "Field Methods to Optimize Capacity and Ensure Storage Containment," by developing and refining the methods used to quantify and optimize $CO_2$ storage resource in major reservoir classes.

### DSF Assessment

The goal of the DSF activities was to use regional-scale models to investigate and refine, as necessary, the method used to quantify $CO_2$ storage resource estimates for a 100-year injection time frame. This study focused on developing results applicable to future widespread commercial-scale $CO_2$ storage operations in which an array of injection wells is used to optimize injection and storage. Two model structural frameworks were created, one flat (structureless) and one with anticlinal structure, each approximately 33.8 $km^2$ (21 miles by 21 miles) with a thickness of 91.4 meters (300 feet). Forty-nine $CO_2$ injection wells were simulated with a spacing of approximately 4.8 km (3 miles). Two depths were investigated, 1219 and 2438 meters (4000 and 8000 feet). Eight facies models were constructed representing ten different depositional environments, including seven clastic depositional environments—eolian, fluvial, deltaic, lacustrine, clastic shelf, clastic strand plain, and clastic slope—and three carbonate depositional environments—carbonate peritidal, carbonate shelf, and reef. Each modeled depositional environment was populated with porosity and permeability distributions based on the Energy & Environmental Research Center's (EERC's) Average Global Database (AGD) for that specific environment. Petrophysical data sets from the AGD used in this work are available on the DOE National Energy Technology Laboratory (NETL) Energy Data eXchange.

This study used closed and semiclosed boundary conditions, as large-scale storage operations using an array of injection wells would cause pressure interference between wells, thus limiting injectivity through closed-system behavior. Storage efficiency values for 1219-meter (4000-foot) depths ranged from 0.29% for carbonate shelf to 0.58% for carbonate peritidal depositional environments, while storage efficiency values for 2438-meter (8000-foot) depths ranged from 0.56% for carbonate shelf to 1.32% for carbonate peritidal depositional environments. The narrow range in $E_{saline}$ values across models, attributable to the closed or semiclosed system boundary conditions, did not distinguish significant differences among depositional environments at the end of 100 years of $CO_2$ injection. This suggests future investigations of prospective storage resource in closed or semiclosed formations may focus less heavily on interpretation of depositional processes through which sedimentary reservoirs were created. However, the results

illustrate the relative importance of depositional environment, formation depth, structural geometry, and boundary conditions on the ***rate*** of $CO_2$ storage in closed or semiclosed systems.

### Hydrocarbon Reservoir Assessment

Estimates of $CO_2$ storage efficiency factors were calculated for $CO_2$ EOR operations using a unique industry database of $CO_2$ EOR sites and 12 different reservoir simulation models. Continuous $CO_2$ injection (CCI) and water alternating gas (WAG) EOR development strategies were considered. Twelve CCI cases were simulated: Cases 1–6 represented clastic fluvial reservoirs, and Cases 7–12 represented carbonate shelf reservoirs. Both clastic and carbonate models were simulated at two different depths (1219 and 2438 meters [4000 and 8000 feet], respectively). Three different reservoir thicknesses were considered at each depth (7.6, 20, and 64 meters [25, 66, and 209 feet], respectively). Six of the twelve cases assessed using CCI simulation were also subjected to simulations of WAG injection. These WAG cases consisted of P50 simulations for Cases 1, 2, and 6 (clastic) and Cases 7, 8, and 12 (carbonate). Altogether, there were 18 simulation cases. In addition to these simulations, a novel statistical modeling technique incorporating the Michaelis–Menten function was used to generate empirical percentile estimates of $CO_2$ storage efficiency factors.

West Texas San Andres dolomite WAG flood performance data were used to derive P10, P50, and P90 $CO_2$ storage efficiency factors of 0.76, 1.28, and 1.74 thousand standard cubic feet per stock tank barrel of original oil in place (Mscf/STB OOIP). Median $CO_2$ storage efficiency factors, expressed on a dimensionless scale, for CCI injection following conventional waterflood varied from 15% to 61% and 8% to 40% for fluvial clastic and shallow shelf carbonate simulation models, respectively, while those from WAG injection varied from 14% to 42% and 8% to 31%, respectively. Variation in the $CO_2$ storage efficiency factors was largely attributable to reservoir depth (a surrogate for reservoir pressure and temperature) and lithology (clastic vs. carbonate reservoirs). The results of this work provide practical information that can be used to quantify $CO_2$ storage resource estimates in oil reservoirs during $CO_2$ EOR operations (as opposed to storage following depletion) and the uncertainty associated with those estimates.

### Discussion and Relevance

The research activities for both DSFs and conventional hydrocarbon reservoirs associated with $CO_2$ EOR supported the development of a best practices manual on optimizing and quantifying $CO_2$ storage resources in these geologic settings. Using lessons learned from this work and other DOE-funded research, approaches outlined in the best practices manual guide the user through a series of decision points to more accurately estimate the $CO_2$ storage resource potential in geologic formations.

# OPTIMIZING AND QUANTIFYING $CO_2$ STORAGE RESOURCE IN SALINE FORMATIONS AND HYDROCARBON RESERVOIRS

## INTRODUCTION

Geologic storage of carbon dioxide ($CO_2$) is being considered as one approach to mitigate the increase in atmospheric concentrations of anthropogenic $CO_2$ from large stationary sources. A thorough understanding of the available $CO_2$ storage resource on a region- or country-wide level is key to the large-scale implementation of this technology. Over the past decade, methods have been developed to estimate $CO_2$ storage resource in both deep saline formations (DSFs) and hydrocarbon reservoirs (U.S. Department of Energy National Energy Technology Laboratory, 2012; Goodman and others, 2011, 2013). DSFs, as defined for $CO_2$ storage, occur at depths generally greater than 800 meters (2625 feet) and have salinities greater than 10,000 ppm total dissolved solids (TDS). $CO_2$ storage in hydrocarbon reservoirs is typically associated with $CO_2$ enhanced oil recovery (EOR), where $CO_2$ is stored in pore space previously occupied by water and hydrocarbons. Both types of geologic $CO_2$ storage require laterally extensive sealing units to contain injected $CO_2$ within the zone(s) of interest. The combination of the reservoir and sealing units together is referred to as the “storage complex” (Canadian Standards Association, 2012).

The aim of this Energy & Environmental Research (EERC) study was to 1) build and expand upon the work of Gorecki and others (2009) and the IEA Greenhouse Gas R&D Programme (IEAGHG) (2009) in refining established methods of storage resource estimation in DSFs on a limited time frame (i.e., 100-year injection period) and 2) increase understanding of the relationship between $CO_2$ storage and EOR, and refine the analytical tools used to assess such operations. Modeling and numerical simulation activities were conducted for each of the two research efforts. Key factors such as depositional environment, structure, and heterogeneity were investigated to determine their impact on storage resource and efficiency.

## BACKGROUND

### Deep Saline Formations

Previously developed methods for estimating $CO_2$ storage in DSFs focused on providing ultimate storage estimates, that is, the amount of $CO_2$ able to be stored in a geologic target at maximum efficiency, based on 1) storage efficiency coefficients specific to generic reservoir lithology classifications (clastics [sandstone], limestone, and dolomite [dolostone]) and 2) an assumption of boundary conditions (i.e., open or closed hydrogeologic systems) (Gorecki and others, 2009; U.S. Department of Energy National Energy Technology Laboratory, 2012; Peck and others, 2014, 2015). However, numerical simulations have shown that it may take hundreds to thousands of years to reach ultimate storage capacity for large-scale $CO_2$ capture and storage (CCS) operations, which is beyond the time frame of interest for mitigating climate change in the next century (IEA Greenhouse Gas R&D Programme, 2014; Bachu, 2015).

Gorecki and others (2009) estimated $CO_2$ storage efficiency coefficients for a variety of DSF depositional environments. Geologic properties of potential $CO_2$ storage reservoirs (DSFs) classified by depositional environment vary less than those based on gross lithology, providing a better predictor of storage efficiency and more accurate estimates of $CO_2$ storage. $CO_2$ storage efficiency factors from Gorecki and others (2009) were created using small models (4 $mi^2$) and simulation time frames of less than 5 years. The current project builds on this earlier work by determining $CO_2$ storage efficiency for regional-scale DSFs using a 100-year time frame.

### Hydrocarbon Reservoirs

Like DSFs, methods have been developed to calculate $CO_2$ storage resource in hydrocarbon reservoirs (Bachu and others, 2007; U.S. Department of Energy National Energy Technology Laboratory, 2007). In general, these methods estimate a volume for the hydrocarbon trap and calculate the mass of $CO_2$ that could be stored within that volume. These methods are limited, however, in their ability to incorporate site-specific operational factors (e.g., utilization factor, recovery factor). The oil and gas industry often uses a mass balance approach to estimate storage capacity in a reservoir, but this approach hinges on estimating the total volume of hydrocarbons extracted from the reservoir at the end of its operational life, a number that fluctuates depending on $CO_2$ retention and sweep efficiency. This project expands on existing methods by integrating operational data from active $CO_2$ EOR projects to develop $CO_2$ storage efficiency factors for oil reservoirs that can be used at the beginning and throughout operations.

## DSF ASSESSMENT

Over the past decade, several studies have developed methods to calculate $CO_2$ storage resource in DSFs—generally deeper than 800 meters (2625 feet) and with salinity greater than 10,000 mg/L—with the goal of providing reliable estimates of the overall $CO_2$ storage resource potential available on a large scale. Previously developed methods have focused on providing storage efficiency estimates classified by a generic lithology (i.e., clastic [sandstone], limestone, and dolomite [dolostone]) and an assumption of hydrogeologic boundary conditions (i.e., open, closed, or semiclosed) (Bachu and others, 2007; Gorecki and others, 2009; Goodman and others, 2011; U.S. Department of Energy National Energy Technology Laboratory, 2015; Peck and others, 2014; Bachu, 2015). Although these methods are useful, storage efficiency values based on generic lithology classifications may not represent the amount of variability in each of these types of rocks, resulting in uncertainty in $CO_2$ storage resource estimates for DSFs. This uncertainty stems from combining a variety of depositional environments into a single lithology classification. For example, fluvio-deltaic formations will likely have different petrophysical properties (e.g., porosity, connected pore volume, or preferential fluid flow patterns) than those deposited during eolian processes because of facies associations, sorting, and rounding. The different physical processes responsible for generating these sedimentary deposits create varying degrees of heterogeneity and, thus, potentially different $CO_2$ storage efficiencies despite being broadly classified as “clastic sandstone formations.” Similarly, reef carbonates (limestone, dolostone) will likely have different petrophysical properties because of facies associations, subaerial exposure and karsting, and diagenesis, when compared with shallow marine shelf carbonates, despite both being broadly classified as “carbonate aquifers” (Koltermann and Gorelick, 1996; Henson and others, 2002; Fitch and others, 2015). In light of this likely variability, a finer-scale approach to estimating $CO_2$ storage efficiencies by subdividing and classifying saline formations according to their unique depositional settings, rather than broad, generic rock types (i.e., sandstone, limestone, and dolostone), may be warranted.

Currently, $CO_2$ storage operations in DSFs are largely subcommercial-scale and research-oriented, employing a relatively small number of wells (e.g., one to two), and most focus primarily on testing technologies used to monitor injected $CO_2$. The aim of this study, however, was to quantify the effects of depositional environment on $CO_2$ storage efficiency and storage rates with relevance to future widespread commercial-scale CCS operations employing a relatively large number of wells. Such operations will likely be designed to maximize the $CO_2$ storage capacity of entire DSFs or at least portions of such formations, meeting the requirements imposed by regulatory entities and sufficient depth to keep $CO_2$ in the supercritical state (~800 meters [2625 feet]). To achieve this goal, regional-scale models were developed representing ten different depositional environments. In this work, the term “depositional environment” implies a particular setting in which a set of physical, chemical, and biological processes operates to generate a certain kind of sedimentary deposit (Boggs, 2001). The petrophysical properties distributed within these models were derived from an updated version of the EERC’s Average Global Database (AGD), a diverse data set of porosity and permeability measurements collected from worldwide reservoirs and classified by depositional environment. The method used in this work was designed to produce models with generic properties reflecting real-world depositional settings, thereby producing globally relevant results for estimating $CO_2$ storage resource potential. Numerical simulations were used to evaluate each geologic model for $CO_2$ storage efficiency and storage rates over an injection time frame of 100 years, which was deemed to be a realistic timescale for operating $CO_2$ storage projects. The results may be used to inform $CO_2$ storage resource estimates for the specific depositional environments examined in this study.

## Geologic Model Construction

To meet the goal of producing results relevant to future widespread commercial-scale CCS operations, formation-scale geologic models were created. However, models at this scale require very large cell sizes to keep the total cell count low enough to allow even high-performance computing technology to complete simulations in a reasonable time frame. The large cell sizes of these models ultimately created intractable challenges in accurately replicating geologic heterogeneity.

To resolve these challenges, a sensitivity analysis was conducted to determine the optimum cell size. The results were then used to inform a proper regional-scale model extent. A 3048 × 3048 × 9.1-meter (10,000 × 10,000 × 30-foot) volume was gridded with multiple cellular resolutions, which included lateral cell dimensions of 15.2, 76.2, 152.4, 228.6, 304.8, 381, 457.2, 533.4, and 609.6 meters (50, 250, 500, 750, 1000, 1250, 1500, 1750, and 2000 feet) and thicknesses of 1.5, 3, 4.6, and 9 meters (5, 10, 15, and 30 feet) (a total of 33 grids created with total cell counts ranging from 240,000 cells in the finest resolution to 25 cells in the coarsest).

A base case grid of 15.2 × 15.2 × 1.5-meter (50 × 50 × 5-foot) cells was established as a starting point because this resolution was fine enough to capture realistic geologic heterogeneity within each of the modeled depositional environments. Porosity and permeability properties were distributed in the base case grid and then upscaled (i.e., averaged) into each of the other coarsened model grids. Porosity was upscaled using an arithmetic mean algorithm, ensuring pore volume remained comparable between the cases. Permeability was upscaled using a geometric mean algorithm, as is appropriate for variables with logarithmic distribution. Each of the gridded volumes were subjected to a 1-year simulation with one $CO_2$ injection well placed in the center of the model grid. An analysis of the simulation results (cumulative $CO_2$ mass injected) indicate that an increase in cell size was accompanied by a decrease in $CO_2$ injection rate (and total injected $CO_2$ mass; Figure 1).

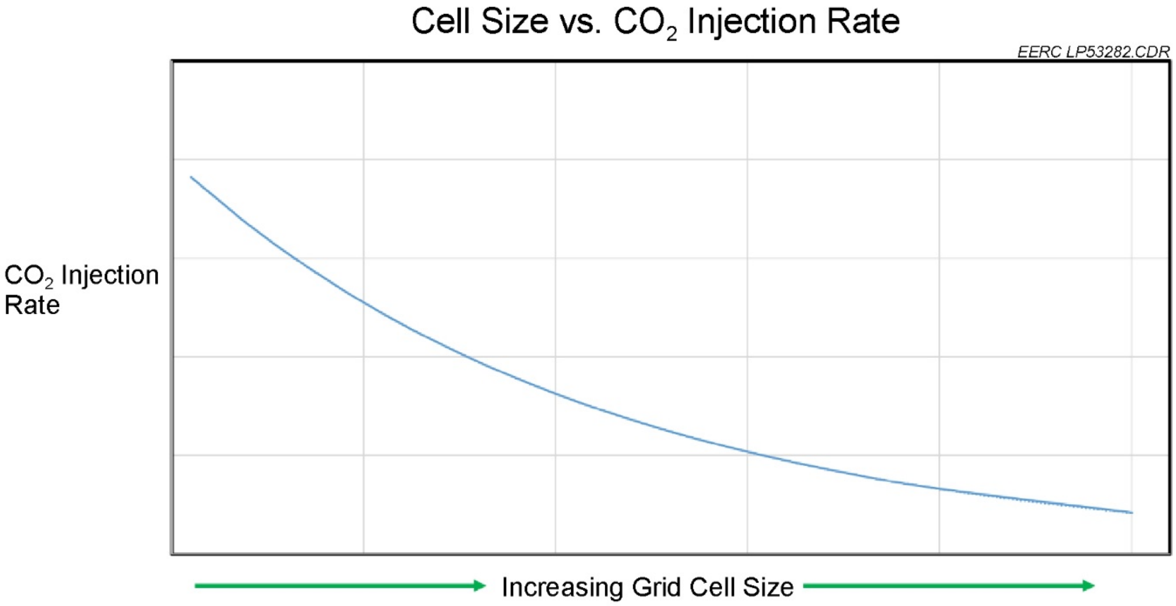

Figure 1. General relationship between cell size and $CO_2$ injection rate.

The trend illustrated in Figure 1 is interpreted as an artifact of the simulation software's calculation of $CO_2$ saturation as a function of $CO_2$ brine relative permeability. $CO_2$ saturation in larger cells tends to build more slowly. $CO_2$ permeability, calculated from $CO_2$ brine relative permeability curves input to the simulation, was "held back" by slowed $CO_2$ saturation buildup in the model grids composed of larger cells.

This inverse relationship between cell size and simulated $CO_2$ injection rate/mass is important for two reasons. The first reason is that, because the regional-scale models planned would be generic rather than based upon a specific location with production/injection data, there would be no history matching in numerical simulation efforts with which this effect could be compensated. If history matching were to be implemented, such an effect might be negated by adjusting the overall permeability distribution or the $CO_2$ brine relative permeability curves. The second reason is that the $CO_2$ injection simulation would be stopping short of achieving ultimate storage capacity. The ultimate storage capacity would likely be similar between each of the different cases, as the results would be closely related to rock compressibility, fluid compressibility, pore volume, and pressure differential (between initial and final pressures), and each of these variables remained similar between the cases. The simulations planned for this investigation were designed to optimize $CO_2$ storage in a 100-year time frame rather than achieving ultimate storage capacity, thus the relationship between cell size and $CO_2$ injection rate/mass would still be a concern.

Results of the cell size sensitivity analysis determined that a cell size of 152.4 × 152.4 × 3 meters (500 × 500 × 10 feet) was to be used in the models prepared for simulation. This size ensured that geologic heterogeneity could be accurately captured, yet allow for efficient computation time. This cell size was then used to calculate an appropriate model extent. An areal extent of 33.8 $km^2$ (21 miles × 21 miles) and a thickness of 91.4 meters (300 feet) was chosen, yielding a total cell count of slightly more than 1.3 million cells. Two grids with these dimensions were created, one flat and a second with anticlinal structure based upon the actual structure of the Nesson Anticline within the Williston Basin.

### *Facies and Petrophysical Property Modeling*

Generic facies distributions were achieved for each of the depositional environments considered in this study. Eight facies models were created (Table 1, Figure 2), each containing at least one reservoir and one poor-reservoir/nonreservoir facies.

Petrophysical property modeling was conducted after the distribution of facies, involving upscaling of the input data themselves. A key consideration for petrophysical property modeling is the scale of the measurement serving as the basis for petrophysical properties, usually a 2.5-centimeter (1-inch)-diameter core plug for routine porosity and permeability tests, and the scale of the cells to which the data are being applied, in this case cells with dimensions of 152.4 × 152.4 × 3 meters (500 × 500 × 10 feet).

Geologic heterogeneity takes place at different scales for different depositional environments. Cells with dimensions of 152.4 × 152.4 × 3 meters (500 × 500 × 10 feet) (or larger, for that matter) may not enable accurate replication of petrophysical characteristics, as variability in such characteristics may occur in a much shorter distance than 152.4 meters (500 feet). For example, an average fluvial channel width may be assumed as approximately 100 meters (330 feet; Gibling, 2006). An average width of this size would be challenging to replicate with larger cells, as any streams modeled would be forced to a larger width even if only one grid cell wide. The heterogeneity present in a realistic fluvial channel cross section, which may include levee, crevasse splay, channel/thalweg, channel margin/wing, and point bar deposits, would be averaged into a single numerical value for both porosity and permeability. However, there are no “hard” (measured) petrophysical data available for a rock volume equivalent to the desired cell size (potentially containing all of these types of deposits together), as it is impractical to extract an intact volume and accurately assess an average porosity or permeability. Statistical support, rather, is placed in creating smaller cells, distributing petrophysical properties informed by core plug measurements that accurately replicate geologic heterogeneity and upscaling/averaging the distributions into coarser cells.

**Table 1. Deep Saline Formation Models Developed in This Study.** The matrix illustrates the different combinations of depositional environments (model components), grid structure, depth, closed/semiclosed boundary systems, and P10/P50/P90 scenarios that were evaluated using numerical simulations of $CO_2$ injection for 100 years.

| Model Name | Model Components | Grid Structure | Depth, m/ft | | Closed | | | Semi-Closed | | |
|---|---|---|---|---|---|---|---|---|---|---|
| | | | 1219/ 4000 | 2938/ 8000 | P10 | P50 | P90 | P10 | P50 | P90 |
| **Eolian** | Eolian<br>Poor reservoir<br>Nonreservoir – cap rock | Flat | X | X | X | X | X | | X | |
| **Fluvio-Deltaic** | Fluvial<br>Deltaic<br>Poor reservoir<br>Nonreservoir – cap rock | Flat | X | X | X | X | X | | X | |
| **Lacustrine** | Lacustrine<br>Poor reservoir<br>Nonreservoir – cap rock | Flat | X | X | | X | | | | |
| **Clastic Shelf** | Clastic shelf<br>Poor reservoir<br>Nonreservoir – cap rock | Flat | X | X | | X | | | | |
| **Strand Plain** | Strand plain<br>Fluvial<br>Poor reservoir<br>Nonreservoir – cap rock | Flat | X | X | | X | | | | |
| **Clastic Slope** | Clastic slope<br>Poor reservoir<br>Nonreservoir – cap rock | Flat | X | X | | X | | | | |
| **Carbonate Shelf-Peritidal** | Carbonate shelf<br>Peritidal<br>Poor reservoir<br>Nonreservoir – cap rock | Flat | X | X | | X | | | | |
| **Reef** | Reef<br>Carbonate shelf<br>Poor reservoir<br>Nonreservoir – cap rock | Flat | | X | | X | | | X | |
| **Eolian** | Eolian<br>Poor reservoir<br>Nonreservoir – cap rock | Anticline | X | X | X | X | X | | X | |
| **Fluvio-Deltaic** | Fluvial<br>Deltaic<br>Poor reservoir<br>Nonreservoir – cap rock | Anticline | X | X | X | X | X | | X | |

The preceding discussion provides the background needed to discuss upscaling of the input data specifically, which was undertaken to create petrophysical data sets valid for the desired cell size (152.4 × 152.4 × 3 meters [500 × 500 × 10 feet]). Two property-upscaling test grids were created, one with 1.52 × 1.52 × 1.5-meter (50 × 50 × 5-foot) cells and another with 152.4 × 152.4 × 3 meters (500 × 500 × 10 feet) cells. Facies models for each of the depositional environments involved in this study were created in the fine-scale grid with 1.52 × 1.52 × 1.5-meter (50 × 50 × 5-foot) cells.

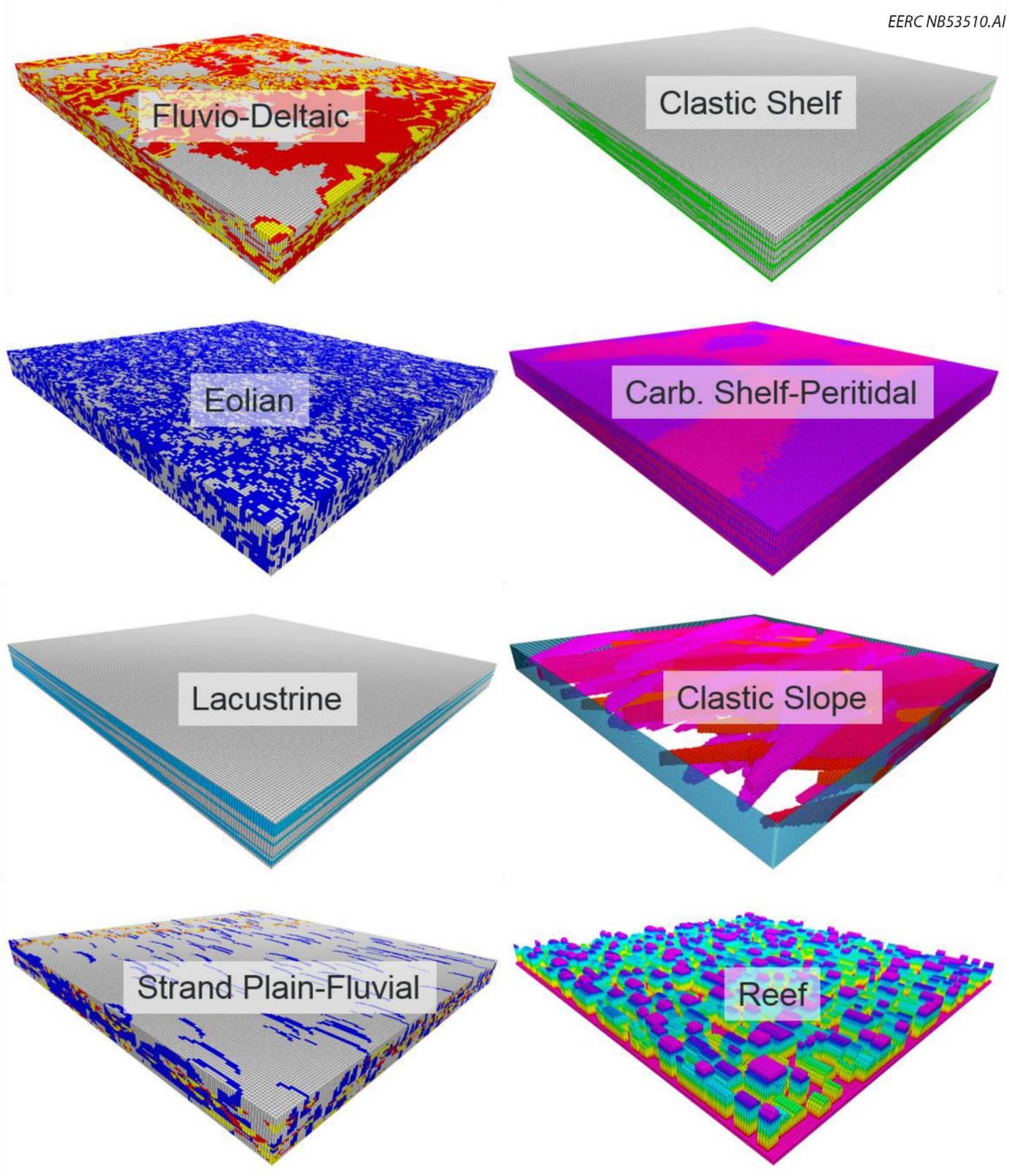

Figure 2. Illustrations of the eight lithofacies models representing ten different depositional environments. The poor-reservoir components of the reef and clastic slope models are not shown to allow visibility of the models' internal structure. Similarly, the caprock component of each of the models has not been shown. Each model is approximately 33.8 km$^2$ (21 miles in length and width) and 91.4 meters (300 feet) in thickness. Vertical exaggerations is 50×.

Petrophysical properties were distributed in the fine-scale grid, the basis of which was the EERC's AGD. Gorecki and others (2009) developed the AGD, which contains a variety of reservoir properties for the primary depositional environments considered in this study, encompassing over 20,000 data points (Figure 3). An important component of the database are porosity–permeability data. These data provide a better understanding of distribution, range, and relationship between these two properties for the depositional environments considered in this study, containing over 600 complete entries representing a variety of international reservoirs. Over 25,000 pairs of porosity–permeability data points were used to geostatistically populate porosity and permeability within the models. The size of the petrophysical data sets used to populate the models did not allow their inclusion as an appendix in this report. However, they are available on the DOE National Energy Technology Laboratory (NETL) Energy Data eXchange.

Variograms used to distribute porosity and permeability were derived from Gorecki and others (2009). The distributed properties were then upscaled into the grid with coarser cells (152.4 × 152.4 × 3 meters [500 × 500 × 10 feet]). The porosity and permeability values resulting from this upscaling process were used to create new porosity–permeability crossplots valid for the desired cell size. Through this process, there is a tendency to lose the extreme values on either end of the histogram, accompanied by a higher frequency of mean values (Figure 4).

The upscaled porosity and permeability data sets were then used to guide petrophysical property distributions in the flat and anticlinal grids (33.8 $km^2$ × 91.4 meters [21 miles × 21 miles × 300 feet]). Petrophysical property uncertainty analyses were conducted in this process, resulting in P10, P50, and P90 petrophysical property distributions. Temperature and pressure properties were also created, representing two different depths: 1219 and 2438 meters (4000 and 8000 feet). These parameters are summarized for each model in Table 2.

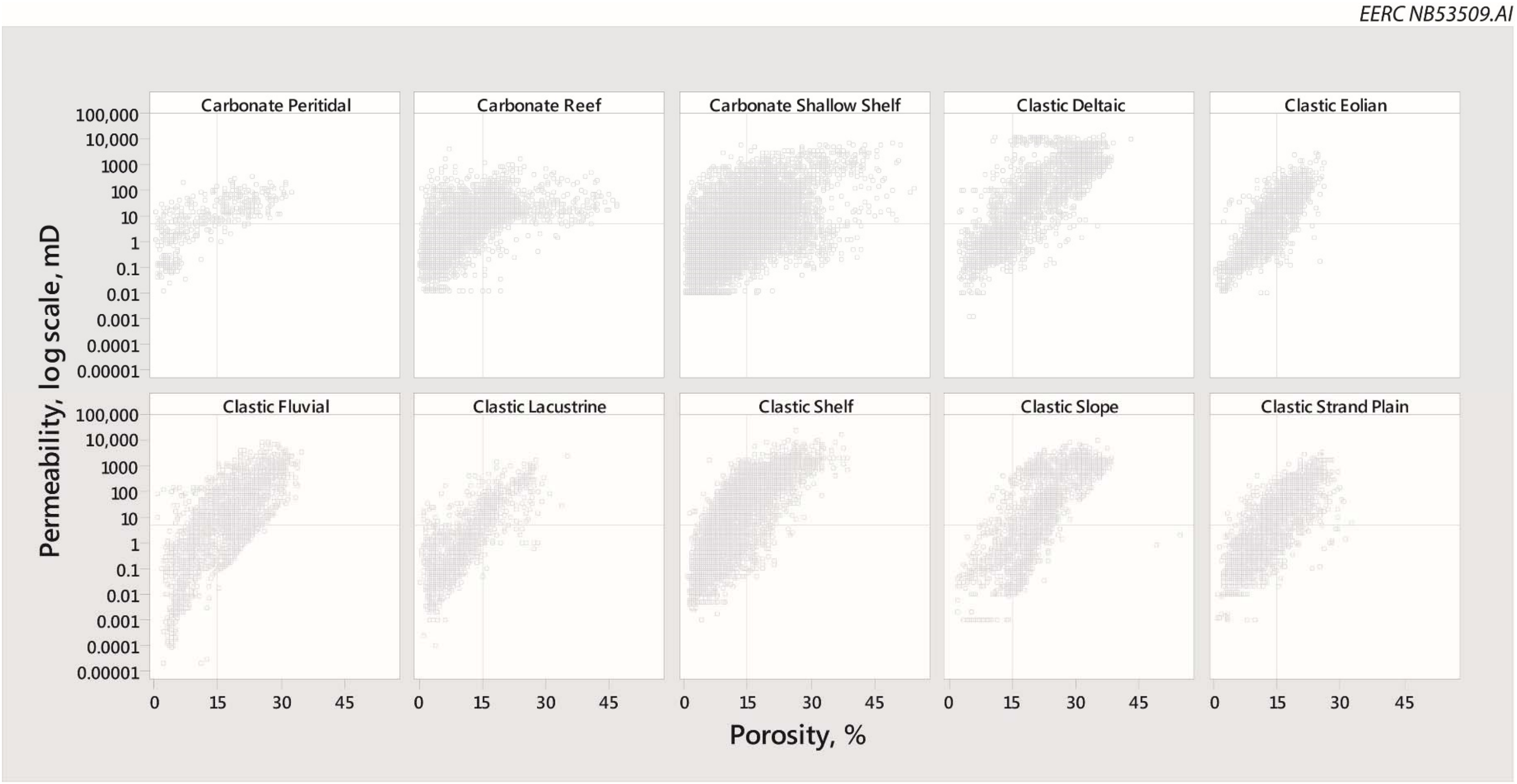

Figure 3. Crossplots of porosity (x-axis) and $\log_{10}$ [permeability] (y-axis) from EERC updated AGD showing the ten different depositional environments modeled in this study. Vertical reference lines at 15% porosity and horizontal reference lines at 5 millidarcies (mD) permeability have been added as a visual aid.

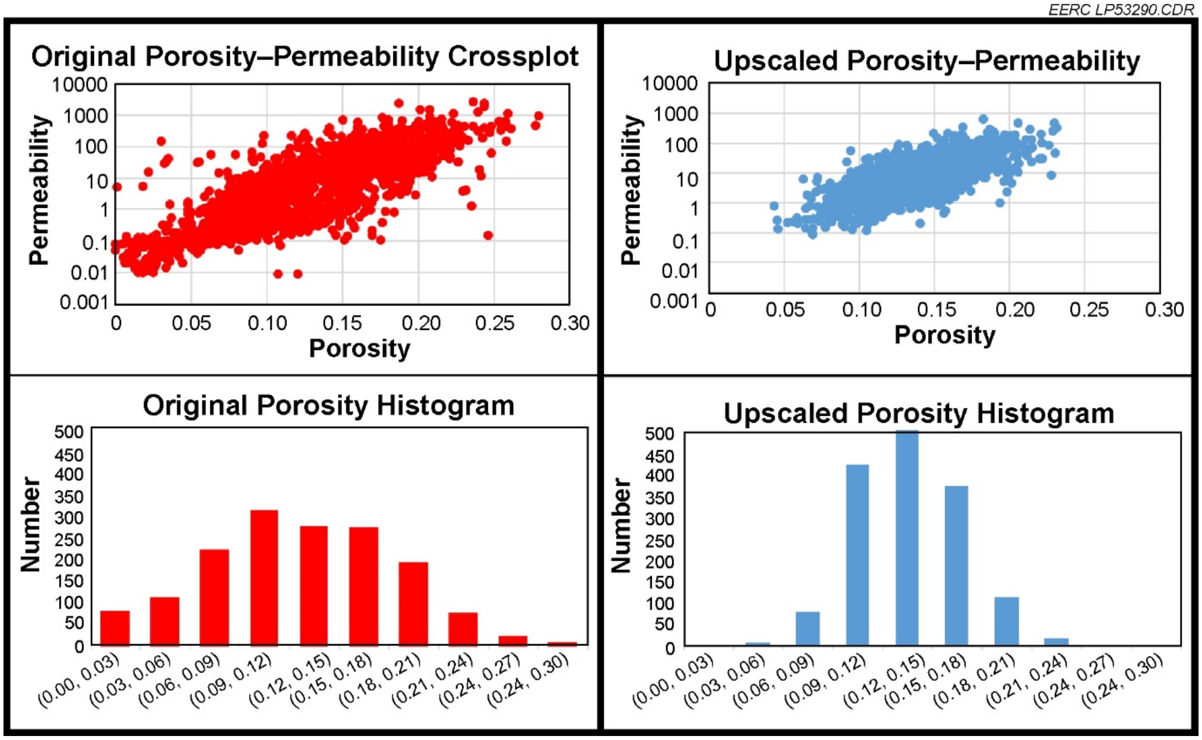

Figure 4. Core plug-measured porosity and permeability data (top left) and a porosity histogram from the same data set (lower left) in comparison to upscaled porosity and permeability data (top right) and an upscaled porosity histogram (lower right). As the degree of upscaling increases (larger grid cells), the data become more averaged, indicated by the higher frequency of midrange histogram values and narrowing of the histogram's range.

**Table 2. Petrophysical Property Statistics from the EERC AGD for Each of the Depositional Environments Considered in This Study**

| | Porosity Statistics, vol/vol | | | | | | Permeability Statistics, mD | | | | | |
|---|---|---|---|---|---|---|---|---|---|---|---|---|
| **Depositional Environment** | **Min.** | **Max.** | **Mean – P10** | **Mean – P50** | **Mean – P90** | **St. Dev.** | **Min.** | **Max.** | **GeoMean – P10** | **GeoMean – P50** | **GeoMean – P90** | **St. Dev.** |
| Carbonate Shallow Shelf | 0.01 | 0.41 | 0.08 | 0.16 | 0.25 | 0.07 | 0.01 | 6342 | 0.96 | 5.57 | 19.95 | 194.77 |
| Reef | 0.01 | 0.41 | 0.07 | 0.15 | 0.23 | 0.06 | 0.01 | 972 | 1.92 | 7.72 | 18.74 | 51.05 |
| Carbonate Peritidal | 0.01 | 0.32 | 0.07 | 0.15 | 0.23 | 0.06 | 0.01 | 313 | 2.15 | 10.24 | 24.25 | 30.78 |
| Clastic Slope | 0.01 | 0.42 | 0.09 | 0.17 | 0.24 | 0.06 | 0.001 | 7336 | 0.43 | 3.64 | 42.76 | 359.28 |
| Fluvial | 0.04 | 0.34 | 0.13 | 0.2 | 0.26 | 0.05 | 0.01 | 1838 | 2.68 | 25.36 | 107.47 | 117.10 |
| Eolian | 0.04 | 0.27 | 0.1 | 0.14 | 0.18 | 0.03 | 0.03 | 702 | 1.97 | 7.59 | 24.58 | 44.87 |
| Clastic Strand Plain | 0.02 | 0.28 | 0.08 | 0.13 | 0.18 | 0.04 | 0.008 | 878 | 1.08 | 4.58 | 18.95 | 51.17 |
| Clastic Shelf | 0.01 | 0.38 | 0.08 | 0.16 | 0.24 | 0.06 | 0.001 | 11,956 | 1.98 | 37.20 | 226.17 | 652.72 |
| Deltaic | 0.02 | 0.42 | 0.13 | 0.21 | 0.29 | 0.06 | 0.01 | 13,206 | 5.62 | 54.27 | 306.47 | 881.51 |
| Lacustrine | 0.01 | 0.33 | 0.06 | 0.13 | 0.2 | 0.05 | 0.0001 | 1698 | 0.37 | 3.86 | 22.73 | 84.49 |

### *Well Placements*

Widespread commercial-scale CCS implementation may require a patterned network of injection wells. Thus a patterned approach to well placement was employed in this study. Previous simulation studies have shown that as $CO_2$ is injected, a plateau is eventually reached where 1) native formation fluids cannot be displaced or compressed further, 2) the limits of reservoir rock compressibility have been reached under operating conditions, and 3) injection wells are shut in to avoid bottomhole pressures high enough to cause fractures (IEA Greenhouse Gas R&D Programme, 2014). The amount of time needed to reach this point depends upon several factors; however, two key factors include the number of wells and the $CO_2$ injection rate. The goal for well placement in this study was to optimize $CO_2$ injection operations over a 100-year time frame. A sensitivity analysis was performed to help determine optimal well spacing/density for the simulations.

To conduct the sensitivity analysis, simulations were run with differing numbers of wells with a maximum injection rate constraint of 2 million tonnes of $CO_2$ per year applied to all wells. Graphical displays of cumulative injected $CO_2$ over time were scrutinized to find a configuration where a plateau was reached in a 100-year time frame. The results of the sensitivity analysis indicated an optimal well placement of 49 injection wells uniformly distributed with a spacing of approximately 4.8 km (3 miles). Although this placement would allow the option of brine production wells (to alleviate pressure buildup between wells), brine extraction was not considered in this study. The specific location for each of the 49 wells was fixed across all geologic models, with the exception of the reef model, to eliminate the variables of well density and placement and allow direct comparison of the simulation results. For the reef model, well placement was optimized to penetrate 49 individual pinnacle reefs. Figure 5 shows the 49-well array using examples with the anticlinal grid and pinnacle reef.

The models included 28 layers to represent the storage portion of the DSF, and two caprock layers (30 layers total). Perforations were set along each wellbore for each of the 28 non-caprock layers.

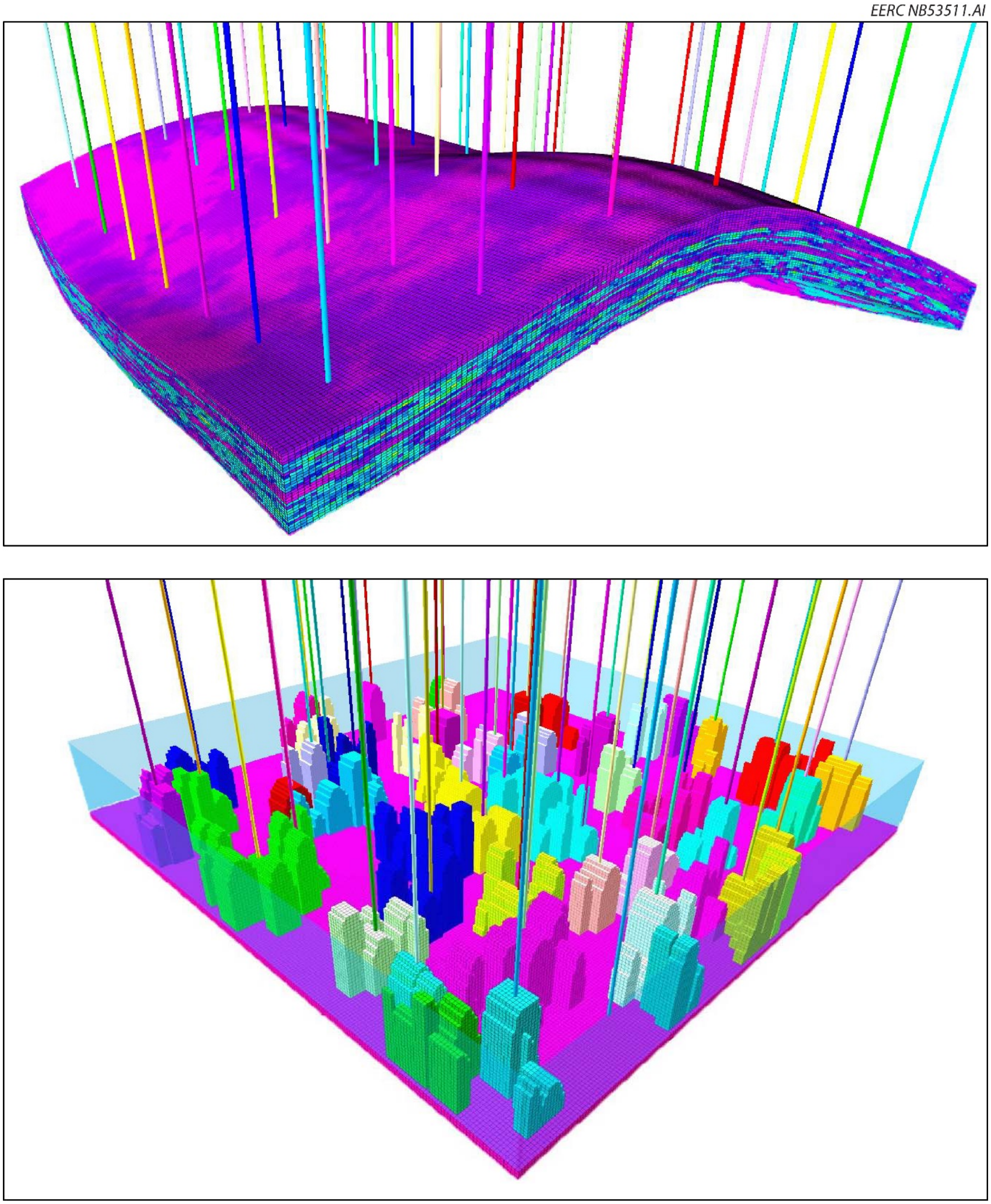

Figure 5. Illustration of the 49-well array shown with the anticlinal grid (top) and pinnacle reef (bottom). Each model is approximately 33.8 km$^2$ (21 miles in length and width) and 91.4 meters (300 feet) in thickness. Vertical exaggerations is 50×. For all but the pinnacle reef models, the specific location for each of the 49 wells was fixed and the well spacing was approximately 4.8 km (3 miles). In the pinnacle reef models, the 49 well locations were optimized to penetrate the 49 largest reef structures, which were assessed by connected reservoir volume.

### DSF Numerical Simulation

Computer Modelling Group, Ltd. Builder (CMG-Builder) was used to populate simulation model parameters and settings, and CMG's GEM (Generalized Equation of State Model Reservoir Simulator) module was used to conduct the numerical simulations.

Models were simulated using temperature and pressure settings representative of two different depths: 1219 and 2438 meters (4000 and 8000 feet). The anticlinal grid had average depths of 1219 and 2438 meters (4000 and 8000 feet), with the hinge and limbs of the structure ranging roughly ±152.4 meters (500 feet) above these depths. The temperature and pressure regimes for the simulation cases were as follows: 1219-meter (4000-foot) depths were 49°C and 11.9 MPa (120°F and 1730 psi); 2438-meter (8000-foot) depths were 82°C and 23.9 MPa (180°F and 3465 psi). These pressure and temperature regimes reflect a linear pressure gradient of 9.8 kPa/meter (0.433 psi/foot) and a linear temperature gradient of 0.027°C/meter (0.015°F/foot) (including a 15.5°C [60°F] surface offset).

A literature review of rock (pore) compressibility values across the depositional environments in Table 1 determined that published estimates were within an order-of-magnitude of each other. Thus a constant value of 5.58E-10 $Pa^{-1}$ (3.85E-06 $psi^{-1}$) was used for all rock types in each model (Newman, 1973; Brady and Lee, 1998; Zhang and others, 2005; Steadman and others, 2010; Henninges and others, 2011; Thibeau and Mucha, 2011; Esken and others, 2012; IEA Greenhouse Gas R&D Programme, 2012; Liu and Li, 2013; Gao and others, 2014).

Boundary conditions of the models were a significant factor in the design of this research and the results. Current storage efficiency estimates for deep saline formations focus on "open" systems (U.S. Department of Energy National Energy Technology Laboratory, 2015). In these systems, which are confined vertically but open laterally, pore space for the injected $CO_2$ is created primarily by lateral displacement of formation water (Bachu, 2015).

A closed system does not permit mass transfer across either vertical or lateral boundaries, and space for the injected $CO_2$ is solely attributable to in situ fluid compressibility and pore dilation (the inverse of compressibility). Closed systems can occur in certain geologic situations where a storage basin is composed of a number of compartmentalized reservoirs laterally separated by low-permeability zones or stratigraphic pinch-outs (Zhou and others, 2008). Storage efficiency and the resulting storage resource estimates based on closed systems represent a conservative end member; many geologic systems will be semiclosed or open and thus permit greater $CO_2$ storage efficiency. In a semiclosed system, the formation does not permit mass transfer across lateral boundaries; however, some fraction of the displaced brine can migrate into and through the overlying sealing unit, which allows for some degree of pressure dissipation, in turn increasing the storage capacity for $CO_2$. The cap rock will not allow $CO_2$ flow because of permeability and capillary barriers (Zhou and others, 2008; Birkholzer and others, 2009; Cavanagh and Wildgust, 2011; Bachu, 2015). The local effect of brine permeation within cap rock is minimal, but other researchers have shown that there may be substantial pressure dissipation due to brine permeation into the overlying cap rock over widespread areas and over long periods of injection (Birkholzer and Zhou, 2009; IEA Greenhouse Gas R&D Programme, 2014).

The simulations in this study focused on closed and semiclosed systems. This decision was made when considering the applicability of simulation results to future commercial-scale $CO_2$ storage operations. Simultaneous injection in an array of relatively closely spaced wells would invariably result in pressure buildup and interference between wells. Only wells along the margins of the well pattern would act in an open manner. Pressure interference between wells in the center of the pattern would cause these wells to experience closed or semiclosed conditions. As mentioned above, the regional-scale modeling approach used in this work can be considered a "unit cell" within a formation-scale CCS operation, bordered on all sides by other unit cells. Pressure buildup and interference between unit cells would cause each cell's boundaries to act closed or semiclosed, affecting even the wells along the margin of the well pattern of the unit cell.

Each of the P50 models were evaluated using closed lateral and vertical boundaries (designated as closed boundary simulation cases in Table 1). P10 and P90 cases for the eolian and fluvio-deltaic models were also simulated in closed-boundary simulations. Only these P10 and P90 cases (eolian and fluvio-deltaic) were chosen because these models, exhibited nearly the worst and best overall model average permeability characteristics, respectively. Simulations were conducted on these end members to illustrate the range of storage efficiency due to petrophysical property uncertainty. In addition, P50 cases for all models were evaluated using semiclosed boundaries (closed lateral boundaries and a lateral confining layer that had non-zero permeability as the top boundary), referred to in Table 1 as the semiclosed boundary simulation cases. This was done to account for brine migration into the cap rock (shale), albeit at a very slow rate. The rate at which pressure can be dissipated (and $CO_2$ injected) is highly sensitive to the shale permeability. The caprock permeability values used in the semiclosed simulations were consistent with those reported by Cavanaugh and Wildgust (2011), ranging from submillidarcy ($10^{-17}$ $m^2$) to subnanodarcy ($10^{-22}$ $m^2$). These low permeability values for the cap rock resulted in semiclosed systems that would be in the closed-range behavior based on prior work conducted by the IEA Greenhouse Gas R&D Programme (IEAGHG) (2014).

A total of 43 $CO_2$ injection simulation cases were run, encompassing the different combinations of depositional environments, depths, P10/P50/P90 scenarios, and closed/ semiclosed boundary systems (Table 1). Each simulation case was run for an injection period of 100 years. Outputs from the numerical simulation models included the total pore volume from the static geologic model, average initial and final formation pressures within the target injection horizon, and the injected $CO_2$ mass for each of the 49 wells at each simulated time step. These outputs were exported to Microsoft Excel for data analysis.

### Data Analysis

The U.S. Department of Energy National Energy Technology Laboratory Atlas V (2015) method of calculating $CO_2$ storage resource for saline formations is shown in Equation 1:

$$G_{CO_2} = A_t\, h_g\, \phi_{tot}\, \rho\, E_{saline} \qquad \text{[Eq. 1]}$$

Where:

$G_{CO_2}$ = $CO_2$ storage resource mass estimate (tonnes).
$A_t$ = Total area (km).

$h_g$ = Gross formation thickness (m).
$\phi_{tot}$ = Total porosity (unitless).
$\rho$ = $CO_2$ density (tonnes/m$^3$).
$E_{saline}$ = Fraction of the total pore volume that will be occupied by the injected $CO_2$.

In this work, values for $E_{saline}$ were derived for each model (overall efficiency) as well as for each depositional environment contained within the model. This was done by dividing the *simulated* mass of stored $CO_2$ by the *total potential* mass of stored $CO_2$ from the static geologic model associated with a specific depositional environment. The total potential mass of stored $CO_2$ was calculated by assessing the total pore volume (taking into account the expansion of pore volume due to pressure increase and rock compressibility/pore dilation) and assuming replacement of all native brine (all pore space) by $CO_2$, the density of which was calculated with the simulated maximum injection pressure constraint (gradient) of 13.6 kPa/m (0.6 psi/ft) (the initial pore pressure gradient assumed was 9.8 kPa/m [0.433 psi/ft]). The $E_{saline}$ coefficients were expressed as a percentage between 0 and 100:

$$E_{saline} = \frac{\text{stored } CO_2 \text{mass (from numerical simulations)}}{\text{total potential mass of stored } CO_2 \text{ (from static geologic model)}} \times 100 \qquad \text{[Eq. 2]}$$

Overall model storage efficiency estimates (reservoir, poor-reservoir, and nonreservoir components together) as well as efficiency values for each individual depositional environment (reservoir components only) using the P50 simulation results were generated for all cases (Table 1). In addition, the P10 and P90 storage efficiency estimates from the closed-boundary simulation cases were used to assess uncertainty and derive a mean and standard deviation via the log-odds normal distribution (Devore, 2004; U.S. Department of Energy National Energy Technology Laboratory, 2015). Since the storage efficiencies may be represented as fractions between 0 and 1, the log-odds normal distribution is appropriate because of its ability to directly integrate the P10 and P90 ranges to derive the mean and standard deviation. As described in detail by DOE NETL (2015), the log-odds normal distribution transforms a fraction, *p*, by Equation 3 and assumes that the transformed variable can be normally distributed:

$$X = \ln\left(\frac{p}{1-p}\right) \qquad \text{[Eq. 3]}$$

where *p* in this case is the storage efficiency obtained according to Equation 2.

The distribution is so named because the $p/(1–p)$ term in Equation 3 is the "odds" for a fraction or probability *p*; therefore, $\ln[p/(1–p)]$ is the "log odds." The transformed variable, *X*, is normally distributed. The *X* value is transformed back to the corresponding *p* value by Equation 4, which is the inversion of Equation 3 (U.S. Department of Energy National Energy Technology Laboratory, 2015):

$$p = \frac{1}{1+e^{-X}} \qquad \text{[Eq. 4]}$$

The log-odds approach thus transforms *p* values of a range into corresponding *X* values of a range. This allows the mean and standard deviation of *X* to be determined from the P10 and P90 simulation results. The mean and standard deviation of *X* fully specify its normal distribution. The mean ($\mu$) and standard deviation ($\sigma$) are calculated from the $X_{10}$ and $X_{90}$ values using relationships between the percentiles and moments of a standard normal distribution (U.S. Department of Energy National Energy Technology Laboratory, 2015):

$$\sigma = \frac{X_{90} - X_{10}}{Z_{90} - Z_{10}} \quad \text{[Eq. 5]}$$

$$\mu = X_{10} - \sigma Z_{10} \quad \text{[Eq. 6]}$$

where $Z_{10}$ and $Z_{90}$ are the $Z$-scores of the 10th and 90th percentiles, respectively, of the standard normal distribution. In this case, $Z_{10}$ equals −1.28 and $Z_{90}$ equals 1.28. It should be noted that the standard deviation is computed first using Equation 5, and this value is then used to compute the mean in Equation 6. Equations 2–6 were used to evaluate uncertainty for the eolian and fluvio-deltaic closed-boundary flat and anticline simulation cases (Table 1).

In addition to evaluating $E_{saline}$, comparisons were made across depositional environments to assess the rates at which $CO_2$ was stored. Dimensionless values were used for these comparisons to express the mass of $CO_2$ as a fraction between 0 and 1 via the following equation:

$$F_t = \frac{M_t}{M_{total}} \quad \text{[Eq. 7]}$$

Where:

$F_t$ = The fraction of total $CO_2$ stored at time "t" (unitless).
$M_t$ = The mass of $CO_2$ stored at time "t" (tonnes).
$M_{total}$ = The total mass of $CO_2$ stored at 100 years (tonnes).

At time = 0 (the start of $CO_2$ injection), $F_t$ is equal to 0, and at time = 100 years (the end of $CO_2$ injection) $F_t$ is equal to 1. Therefore, $F_t$ places all simulation results onto a common dimensionless scale to permit comparisons across depositional environments.

## Results and Discussion

Across the closed-boundary simulation results, the P50 $E_{saline}$ coefficients for the *overall* model (primary depositional environment, poor-reservoir, and caprock components together) for the 1219- and 2438-meter (4000- and 8000-foot) flat structure models were 0.42% ± 0.01% and 0.83% ± 0.02%, respectively, with no significant differences among models. This narrow range in $E_{saline}$ values across all models was observed because 1) each model had total pore volumes within the same order-of-magnitude; 2) the same native formation fluids were assumed for each model (similar fluid compressibility); 3) the same rock compressibility value was assumed for each model; 4) similar bottomhole pressure constraints were assumed for each model, resulting in similar $\Delta p$ or change from initial to final formation pressure; and 5) closed lateral boundary conditions were assumed in each simulation. As previously described, space for the injected $CO_2$ in a closed system is solely attributable to water compressibility and pore dilation. As described in Zhou and others (2008):

$$E_{saline} = (\beta_p + \beta_w)\Delta p \quad \text{[Eq. 8]}$$

Where $\beta_p$ and $\beta_w$ are the pore and water compressibility, respectively, and $\Delta p$ is the difference between initial and final pressure in the target injection horizon.

Pore compressibility for all models was 3.85E-06 $psi^{-1}$ (5.58E-10 $Pa^{-1}$). The $\Delta p$ for the 1219- and 2438-meter (4000- and 8000-foot) flat-structure models was 4.4 and 8.7 MPa (639 and 1255 psi), respectively. Assuming a water compressibility of 4.0E-10 $Pa^{-1}$ (2.8E-6 $psi^{-1}$) (Birkholzer and others, 2009; Bachu, 2015), Equation 8 results in estimated $E_{saline}$ values for the 1219- and 2438-meter (4000- and 8000-foot) flat-structure models of 0.42% and 0.83%, respectively, which is consistent with the simulation results.

As previously discussed, all models contained multiple facies (i.e., reservoir, poor-reservoir, and cap rock), with some models representing multiple depositional environments in the reservoir facies (e.g., fluvio-deltaic). Table 3 summarizes the $CO_2$ storage efficiency values obtained for each depositional environment at 100 years of $CO_2$ injection. When parsing the efficiencies of each model into contributions by individual depositional environments (e.g., fluvial efficiency separate from deltaic efficiency), more notable differences were seen. For example, storage efficiency values for 1219-meter (4000-foot) depths ranged from 0.29% for carbonate shelf to 0.58% for carbonate peritidal depositional environments; while storage efficiency values for 2438-meter (8000-foot) depths ranged from 0.56% for carbonate shelf to 1.32% for carbonate peritidal depositional environments (Table 3).

**Table 3. $E_{saline}$ Results at 100 years of $CO_2$ Injection Summarized by Depositional Environment and Grid Structure for Closed and Semiclosed Boundary Simulations.** Simulation results were not generated for the reef depositional environment at 1219 meters (4000 feet) (N/A).

| | | **$E_{saline}$ (%) at 100 Years** | | | | | | | |
|---|---|---|---|---|---|---|---|---|---|
| | | **1219-m (4000-ft) Depth** | | | | **2438-m (8000-ft) Depth** | | | |
| **Depositional Environment** | **Grid Structure** | **Closed** | | | **Semiclosed** | **Closed** | | | **Semiclosed** |
| | | **P10** | **P50** | **P90** | **P50** | **P10** | **P50** | **P90** | **P50** |
| Eolian | Flat | 0.49 | 0.50 | 0.49 | 0.56 | 0.97 | 0.98 | 0.97 | 1.17 |
| Fluvial | Flat | 0.31 | 0.35 | 0.36 | 0.38 | 0.68 | 0.76 | 0.75 | 0.86 |
| Deltaic | Flat | 0.57 | 0.53 | 0.50 | 0.58 | 1.11 | 1.00 | 0.96 | 1.13 |
| Lacustrine | Flat | | 0.51 | | | | 1.03 | | |
| Clastic Shelf | Flat | | 0.54 | | | | 1.06 | | |
| Strand Plain | Flat | | 0.40 | | | | 0.80 | | |
| Clastic Slope | Flat | | 0.51 | | | | 1.00 | | |
| Carbonate Shelf | Flat | | 0.29 | | | | 0.56 | | |
| Peritidal | Flat | | 0.58 | | | | 1.19 | | |
| Reef | Flat | | N/A | | | | 1.32 | | 1.52 |
| Eolian | Anticline | 0.50 | 0.54 | 0.56 | 0.62 | 1.00 | 1.02 | 1.01 | 1.18 |
| Fluvial | Anticline | 0.36 | 0.46 | 0.47 | 0.50 | 0.70 | 0.87 | 0.88 | 0.96 |
| Deltaic | Anticline | 0.61 | 0.60 | 0.61 | 0.66 | 1.13 | 1.08 | 1.09 | 1.18 |

Formation depth, a proxy for pressure and temperature conditions, had a significant effect on storage efficiency. The deeper 2438-meter (8000-foot) models had roughly 100% greater storage efficiency across all depositional environments (Table 3). Since the pore volumes were roughly equivalent between the 1219- and 2438-meter (4000- and 8000-foot) models, this higher storage efficiency for deeper models is largely attributable to a greater change from initial to final pressure (greater $\Delta p$). The maximum injection pressure constraint (gradient) was 13.6 kPa/m (0.6 psi/ft); therefore, the deeper models permitted greater $CO_2$ injection rates and volumes over the 100-year period.

The anticline models resulted in greater storage efficiency than the flat-model counterparts. For example, the P50 $E_{saline}$ coefficients for the 1219- and 2438-meter (4000- and 8000-foot) anticline eolian models were 0.54% and 1.02%, respectively, which was an increase of 8% and 4% over their flat-model counterparts. This structural geometry effect was greatest for the fluvial depositional environments. The P50 $E_{saline}$ coefficients for the 1219- and 2438-meter (4000- and 8000-foot) anticline fluvial depositional environments were 0.46% and 0.87%, respectively, which was an increase of 31% and 14% over their flat-model counterparts (Table 3). This structural geometry effect for anticline models is likely attributable to 1) greater $\Delta p$ along the deeper limbs of the anticline allowing a greater amount of $CO_2$ to be injected and 2) buoyancy and the tendency of $CO_2$ to rise within the injection horizon into the crest (hinge) of the anticline, which resulted in the available pore space more efficiently filling with $CO_2$ over the injection period.

The additional storage from pressure dissipation in the semiclosed models resulted in slightly greater storage efficiency than their closed-model counterparts. For example, the P50 $E_{saline}$ coefficients for the 1219-meter (4000-foot) flat eolian, fluvial, and deltaic depositional environments for closed-boundary models were 0.50%, 0.35%, and 0.53%, respectively. However, the P50 $E_{saline}$ coefficients for the semiclosed models for these three environments were 0.56%, 0.38%, and 0.58%, respectively, for an increase of approximately 12%, 9%, and 9%, respectively. Similar magnitudes of the semiclosed boundary effect were observed for the 2438-meter (8000-foot) models and for the anticline models (Table 3). The magnitudes of change in storage efficiency between the closed and semiclosed models were small because, as previously discussed, the caprock permeability values used in the semiclosed simulations were in the submillidarcy ($10^{-17}$ $m^2$) to subnanodarcy ($10^{-22}$ $m^2$) range, resulting in semiclosed systems which behaved similarly to closed-boundary systems.

### *Effect of Porosity–Permeability Distribution on Storage Efficiency and Rates*

Figure 4 shows histograms of $CO_2$ storage efficiency at 100 years of $CO_2$ injection for the fluvial depositional environment of the 1219-meter (4000-foot) depth flat and anticline models. Similar results were observed for the 2438-meter (8000-foot) models (figures not shown). These histograms were generated from the P10 and P90 outputs from Table 3 and the log-odds method using Equations 4, 5, and 6, and Monte Carlo simulation. As described above, the porosity–permeability distribution has a large effect on the connected volumes and overall pore volume, with the P10 case having less primary storage facies and less total pore volume and the P90 case containing more of the primary storage facies and greater pore volume. Consequently, uncertainty in the porosity–permeability distribution has an effect on the simulated $CO_2$ storage efficiency. As shown in Figure 6, the range in $CO_2$ storage efficiency (minimum to maximum) was approximately

0.25% to 0.40% for the flat structural model and 0.30% to 0.55% for the anticline structural model. This variability in the simulated $CO_2$ storage efficiency coefficient reflects the uncertainty in the underlying porosity–permeability distribution, which in this case was modeled using the 10 and 90 percent probability range from AGD for eolian, fluvial, and deltaic depositional environments.

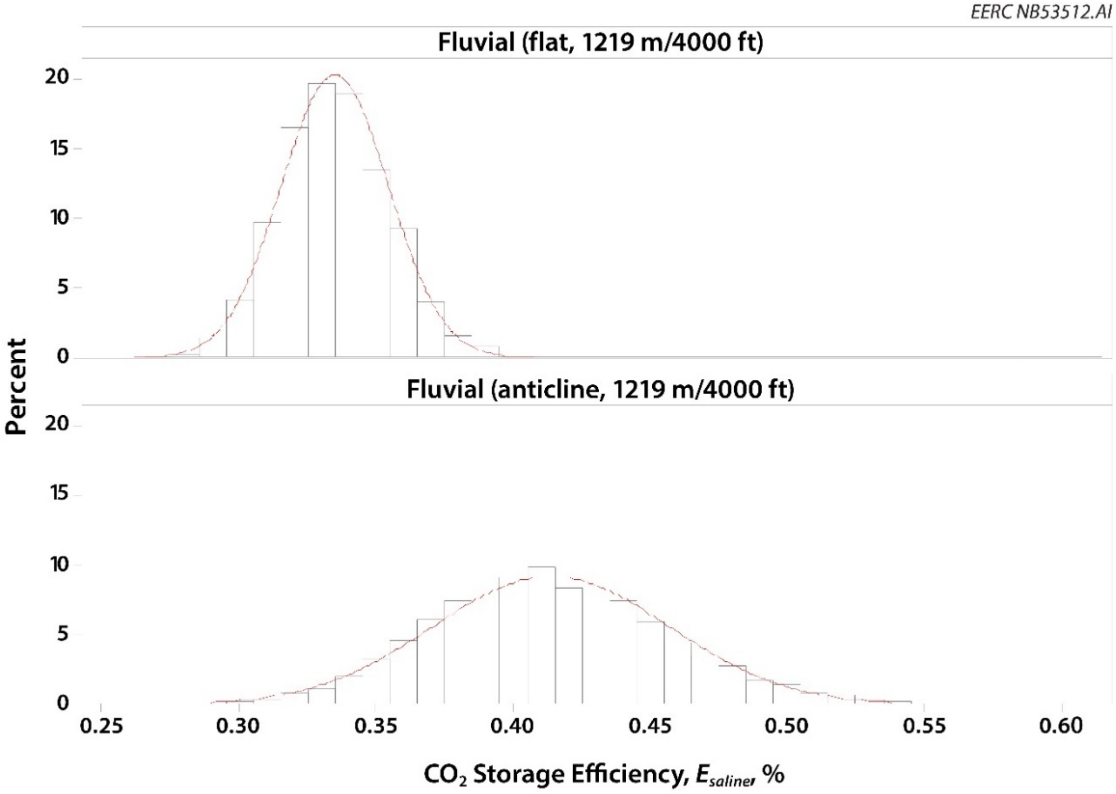

Figure 6. Histograms $CO_2$ storage efficiency (percent, x-axis) for the fluvial depositional environment 1219-meter (4000-foot) flat models (top row) and anticline models (bottom row). These histograms were generated using the P10 and P90 outputs from Table 3 and the log-odds method using Monte Carlo simulation and Equations 4, 5, and 6.

The uncertainty analysis illustrated in Figure 6 underscores the importance of geologic characterization, as variability in petrophysical properties may impact $CO_2$ storage resource estimates. Different types of geologic formations contain varying degrees of heterogeneity, but all tend to have significant heterogeneity at the basin scale. A formation may encompass deposits from multiple depositional environments. For instance, a sandstone formation may contain elements of both fluvio-deltaic and nearshore deposition. In addition, close investigation into any two geologic formations interpreted as being genetically similar, for instance, carbonate shelf and peritidal sequences, will likely reveal significant differences in facies proportions. Other modes of heterogeneity may be due to any number of processes, such as change in water depth at the time of deposition, change in sediment composition and sedimentation rate, differential erosion, diagenesis, and structural complications. All of these factors create heterogeneity in storage resource quality and capacity. Therefore, thorough geologic characterization is needed to constrain estimates of petrophysical properties within DSF and to map the distribution and extent of good and bad reservoir facies proportions within each specific depositional environment.

### *Evaluating $CO_2$ Storage Rates Across Depositional Environments*

Figure 7 shows time series plots for the fraction of $CO_2$ stored over the 100-year injection period for the different depositional environments, structural geometries (flat or anticline), and boundary conditions (closed or semiclosed). Each of these curves exhibited a sigmoidal shape, with an initially slow increase in the fraction of $CO_2$ stored followed by a period of rapid increase and finally tapering toward a fraction of 100%. Comparing results for flat models among depositional environments (top row in Figure 7) showed a consistent order for the time at which the fraction of $CO_2$ increased. The clastic shelf curves increased at the earliest time (the curves farthest to the left), with the eolian and reef curves increasing at the latest time (the curves farthest to the right). The order, from fastest to slowest rate of fractional $CO_2$ storage, was clastic shelf > fluvio-deltaic > clastic slope > carbonate peritidal > clastic strand plain > lacustrine > eolian > reef; however, the carbonate peritidal and clastic strand plain models were virtually indistinguishable, as were the eolian and reef models. These orders were preserved in the 2438-meter (8000-foot) models; however, the effects were diminished (i.e., less separation between the different curves).

The differences in $CO_2$ storage rates are largely attributable to differences in the average porosity and permeability for the different depositional environments. As shown in Figure 8, the fluvio-deltaic and clastic shelf environments had the greatest porosity and permeability, and also the fastest time to store 50% of the total injected $CO_2$. Because of their higher permeability and thus greater ability to convey injected $CO_2$, these systems reached their $\Delta p_{max}$ fastest. Thus an inverse relationship, albeit with weak correlation, was observed between petrophysical property characteristics and the rate with which $CO_2$ injection occurred. As both porosity and permeability properties decreased, the amount of time needed to store 50% of the total $CO_2$ mass increased. Injected $CO_2$ must travel farther to find the necessary void volume for storage in a scenario with decreased pore volume in comparison to a scenario with greater pore volume, assuming similar amounts of $CO_2$ being injected in both cases. This suggests a "tighter" (less permeable) formation may result in a $CO_2$ plume of greater areal extent, instead of the low-permeability rock simply keeping the $CO_2$ plume condensed through resistance to flow, and this process takes place more slowly than in formations with better petrophysical characteristics.

In addition, a general trend of increasing $CO_2$ injection rate was noted as depth increased. The deeper models, with more pressure space available during injection (greater $\Delta p$), received $CO_2$ at a higher rate simply because of injection could take place at higher pressures.

As shown in Table 3 and described above, at the end of the 100-year $CO_2$ injection period, the anticline models had greater storage efficiency than the flat-model counterparts. However, the anticline models had somewhat slower rates of $CO_2$ storage than the flat models (i.e., the solid curves lie to the right of the dotted curves in the middle panels of Figure 7). This was especially true for the final 20% of $CO_2$ stored ($F_t = 0.8$ to 1.0) in the fluvio-deltaic models. For example, the fluvio-deltaic 1219-meter (4000-foot) flat model took 0.8 years to reach $F_t = 0.5$, while the anticline model took 1.0 year, for an increase of a factor or 1.25.

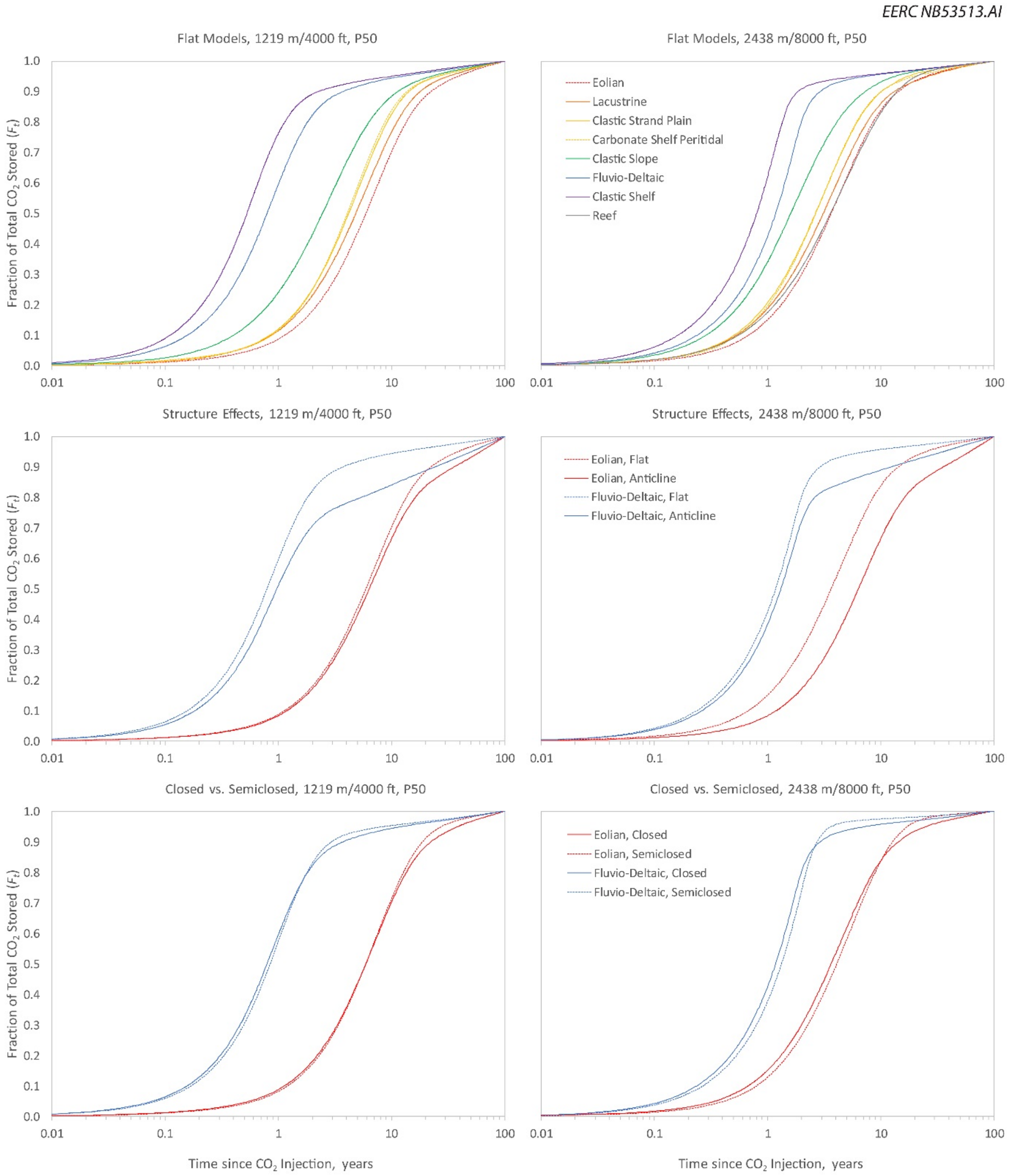

Figure 7. Time series plots for the fraction of CO2 stored (Ft, y-axis) over the 100-year injection period (x-axis) for the different models. The left and right columns show results for the 1219- and 2438-meter (4000- and 8000-foot) models, respectively. The top panels show the P50 results for closed boundary flat models. Simulation results were not generated for the reef depositional environment at 1219 meters (4000 feet). The middle panels compare the P50 results for the closed boundary flat and anticline models. Lastly, the bottom panels compare the P50 results for the closed and semiclosed boundary flat models.

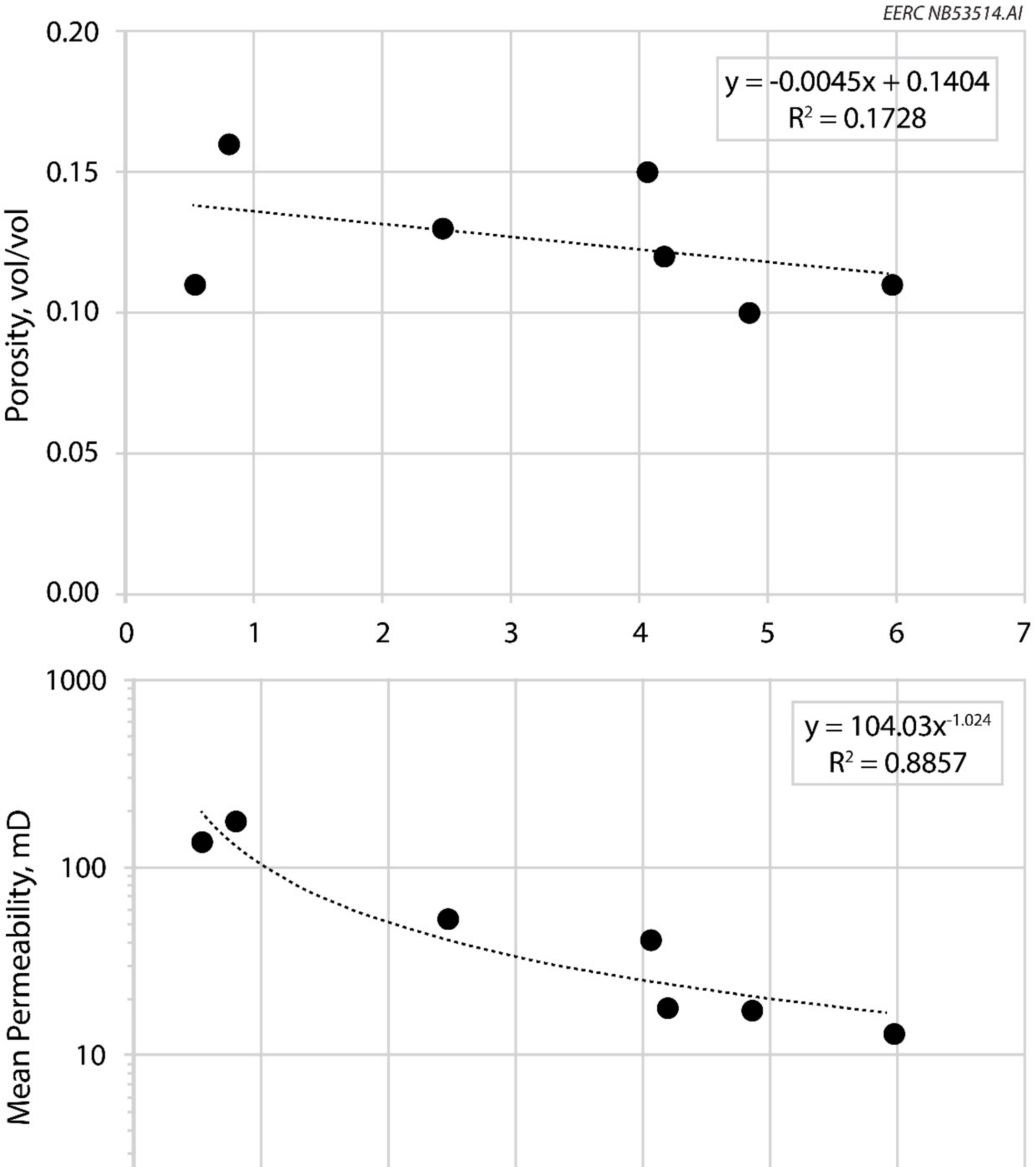

Figure 8. Time series plots showing the inverse relationships between models' average porosity (top) and average permeability (bottom) characteristics and the time to inject 50% of the total $CO_2$ storage capacity.

The rates of $CO_2$ storage were virtually indistinguishable between the closed and semiclosed boundary models within the same depositional environment for *most* of the $CO_2$ injection period. Virtually no significant difference was noted in the time to reach $F_t = 0.5$ between closed and semiclosed models, regardless of formation depth, structural geometry, or depositional environment (Figure 9). However, the semiclosed models had marginally slower rates for the final 10% of $CO_2$ stored ($F_t = 0.9$ to 1.0) (i.e., the solid curves lie to the right of the dotted curves in the bottom panels of Figure 7 when the *y*-axis is greater than approximately $F_t = 0.9$). The pore volumes were equivalent between closed and semiclosed models of the same depositional environment. In addition, the cap rock (seal) in the semiclosed models did not allow $CO_2$ flow because of permeability and capillary barriers and, therefore, only allowed pressure dissipation via brine displacement. Since bottomhole injection pressure was limited to the fracture pressure, the rates of $CO_2$ storage were nearly identical between the closed and semiclosed boundary models for the majority of the $CO_2$ injection period. However, the pressure dissipation provided by the semiclosed boundary resulted in additional storage and, therefore, slower rates for the final 10% of $CO_2$ stored.

Figure 9 shows bar charts of the time in years for each simulation to reach 50% of the total $CO_2$ mass injected ($F_t = 0.5$). These comparisons elucidate the relative importance of depositional environment, formation depth, structural geometry, and boundary conditions on the rate of $CO_2$ storage. For example, among the 1219-meter (4000-foot) depth, flat models, it took 0.5 years for the clastic shelf model to reach $F_t = 0.5$, but it took the eolian model six years, or 12 times longer. Therefore, while the $CO_2$ storage efficiency at the end of the 100-year injection period was nearly identical between these two depositional environments (0.43% vs. 0.42%), the rates at which these formations accepted their total mass of $CO_2$ differed significantly.

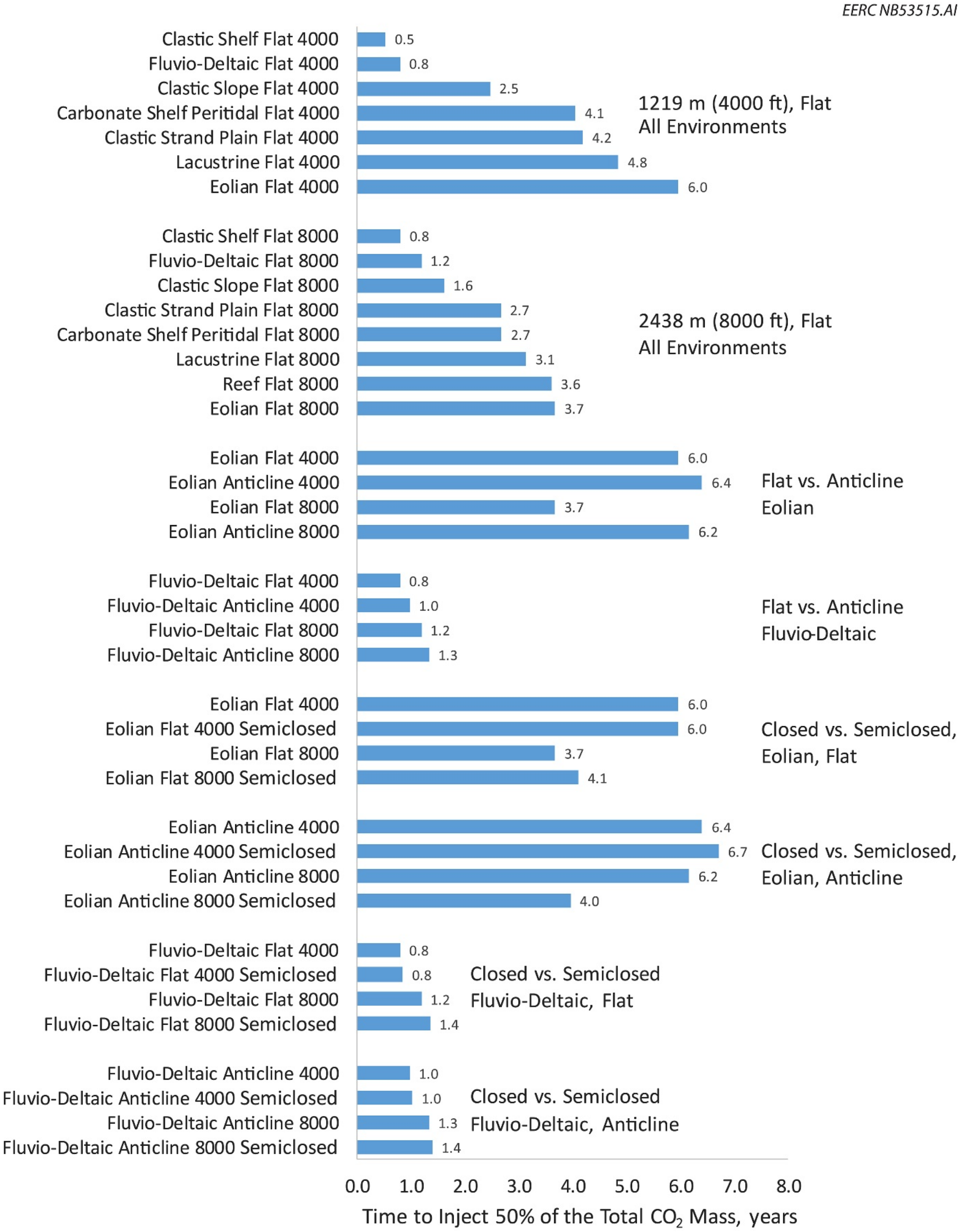

Figure 9. Bar charts comparing the time to inject 50% of the total $CO_2$ mass (x-axis) for the different model combinations.

### *Comparisons to IEAGHG (2014)*

In 2014, IEAGHG commissioned the EERC to develop storage coefficients for $CO_2$ storage in DSFs. The project was cosponsored by DOE (IEA Greenhouse Gas R&D Programme, 2014). The IEAGHG (2014) approach compared volumetric and dynamic $CO_2$ storage efficiencies in an open system, represented by the Minnelusa Formation, and a closed system represented by the Qingshankou and Yaojia Formations. The results provided low and high estimates as a function of time, from 50 years to 2000 years of $CO_2$ injection.

Table 4 compares the IEAGHG (2014) results to the overall model storage efficiencies from the current work. As shown in the table, the average storage efficiencies at 100 years for the 1219-meter (4000-foot) models (0.42%) and 2438-meter (8000-foot) models (0.83%) from the current study were comparable to the dynamic storage efficiencies for the Minnelusa Formation at 50 years and for the Qingshankou and Yaojia Formations at 500 years or more of $CO_2$ injection. The open hydrogeologic systems of the Minnelusa Formation permitted greater storage efficiency over time (up to 18% at 2000 years of injection), which as previously described was a function of additional $CO_2$ storage associated with lateral brine displacement, as opposed to being limited to the water compressibility and pore dilation.

**Table 4. Comparison of $E_{saline}$ Results (percent) from IEAGHG (2014) for the Minnelusa and Qingshankou–Yaojia Systems to the Overall Model $E_{saline}$ Results from the Current Work**

| | Minnelusa System | | Qingshankou–Yaojia System | | Current Work Overall Model, m/ft | |
|---|---|---|---|---|---|---|
| **Point of Comparison** | **Low** | **High** | **Low** | **High** | **1219/4000** | **2438/8000** |
| Volumetric Efficiency (closed system) | 0.54% | 0.54% | 0.21% | 0.21% | NA | NA |
| Volumetric Efficiency (open system) | 2.90% | 11.00% | 1.30% | 10.00% | NA | NA |
| Dynamic Efficiency (50 years of injection) | 0.55% | 1.70% | 0.28% | 0.40% | NA | NA |
| Dynamic Efficiency (100 years of injection) | NA | NA | NA | NA | 0.42% | 0.83% |
| Dynamic Efficiency (200 years of injection) | 1.90% | 4.30% | 0.39% | 0.52% | NA | NA |
| Dynamic Efficiency (500 years of injection) | 2.50% | 7.90% | 0.45% | 0.60% | NA | NA |
| Dynamic Efficiency (2000 years of injection) | 3.40% | 18.00% | 0.62% | 0.72% | NA | NA |

## HYDROCARBON RESERVOIR ASSESSMENT

Among hydrocarbon-bearing formations, one proven technology that both produces oil and, through the process, permanently stores $CO_2$ in the subsurface is $CO_2$ EOR. $CO_2$ EOR refers to the process whereby an operator injects $CO_2$ into the subsurface at an oil field, after which it mixes with the oil to swell it and reduce the oil viscosity, making it lighter and detaching it from the rock surfaces. These subsurface alterations cause the oil to flow more freely within the reservoir so that it will flow to production wells. During this process, approximately 50% of the total volume of injected $CO_2$ (purchased plus recycled) is produced together with oil, separated, and reinjected, but nearly all (>95%) of the purchased $CO_2$ delivered to the oil field remains securely trapped within the geologic formation (Melzer, 2012; Azzolina and others, 2015).

$CO_2$ EOR occupies an important place in the realm of geologic $CO_2$ storage, as it is likely to be the primary means of geologic $CO_2$ storage during the early stages of commercial deployment because the value of the produced oil offsets some of the costs of CCS (Peridas, 2008; Leach and others, 2011). As of 2014, there were 136 active $CO_2$ EOR projects identified in the United States (Koottungal, 2014), with forecasts predicting strong future growth (Kuuskraa and Wallace, 2014). Besides the United States, China, Indonesia, and other countries have expressed strong interest in using $CO_2$ EOR for climate change mitigation. $CO_2$ storage resource estimates for new and ongoing $CO_2$ EOR operations will help to quantify the amount of carbon storage potential available through this process.

The DOE methodology for estimating the $CO_2$ storage resource in oil reservoirs uses a volumetric approach and the standard industry method to calculate original oil in place (OOIP) (Calhoun Jr., 1982; Lake, 1989). Equation 9 provides the general form of the volumetric equation to calculate the $CO_2$ storage resource mass estimate ($G_{CO2}$) for geologic storage in oil reservoirs (U.S. Department of Energy National Energy Technology Laboratory, 2012):

$$G_{CO2} = A\, h_n\, \phi_e\, (1 - S_{wi})\, B\, E_{oil}\, \rho_{CO2} \qquad \text{[Eq. 9]}$$

Where (M = mass; L = length):

$G_{CO2}$ = Mass estimate of oil and gas reservoir $CO_2$ storage resource (M).
$A$ = Reservoir area ($L^2$).
$h_n$ = Net thickness (L).
$\phi_e$ = Average effective porosity ($L^3/L^3$).
$(1 - S_{wi})$ = (1 – initial water saturation) ≡ original hydrocarbon saturation ($L^3/L^3$).
$B$ = Oil formation volume factor (stock tank barrel [STB]/reservoir barrel [RB]) ($L^3/L^3$).
$E_{oil}$ = $CO_2$ storage efficiency factor ($L^3/L^3$).
$\rho_{CO2}$ = $CO_2$ density ($M/L^3$).

In Equation 9, the product of $A$, $h_n$, $\phi_e$, $(1 - S_{wi})$, and $B$ yield the OOIP (red-colored text in Equation 9. For the $CO_2$ storage resource estimate at reservoir depletion, the factor $E_{oil}$ is equivalent to the incremental oil recovery factor (*RF*), (Bachu and others, 2007). A critical insight, and a major component of the work presented in this study, is that in oilfield terms, the *RF* and the $CO_2$ net utilization factor ($UF_{net}$) together represent the $CO_2$ storage efficiency factor, $E_{oil}$, for $CO_2$ storage in $CO_2$ EOR operations, as opposed to $CO_2$ storage following reservoir depletion. Thus Equation 9 may be rewritten as:

$$G_{CO2} = OOIP \times RF \times UF_{net} \times \rho_{CO2} \qquad \text{[Eq. 10]}$$

Where:

*OOIP* = Original oil in place (stock tank barrel [STB]).
*RF* = Incremental oil recovery factor in $CO_2$ EOR (%OOIP).
$UF_{net}$ = $CO_2$ net utilization factor (Mscf [thousand standard cubic feet]/STB).
$\rho_{CO2}$ = $CO_2$ density, with a conversion factor of 1 tonne $CO_2$ per 19.25 Mscf at normal conditions (U.S. Department of Energy National Energy Technology Laboratory, 2010).

In Equation 10, the red- and blue-colored text identifies the common components with Equation 9. The form of Equation 10 provides a more tractable volumetric equation because OOIP, *RF*, and $UF_{net}$ are common performance metrics. Incremental oil recovery in this work represents oil that is produced following the primary and secondary oil production, i.e., during tertiary recovery from the $CO_2$ flood and, hence, incrementally adds to the entire oil production from the oil reservoir. Incremental oil recovery is expressed as a dimensionless variable, the incremental oil *RF*, which is expressed in units of %OOIP. Industry commonly expresses the $CO_2$ net utilization factor ($UF_{net}$) as the amount of purchased $CO_2$ used to recover a barrel of oil, in units of thousand standard cubic feet (Mscf)/STB. $CO_2$ net utilization does not include the recycled $CO_2$ component and, therefore, only incorporates the new, purchased $CO_2$ volumes into the calculation.

Among the parameters in Equation 10, *RF* is already normalized to the reservoir volume because it is expressed in units of %OOIP. Similarly, $UF_{net}$ scales purchased $CO_2$ use to barrels of oil produced and, therefore, the units of Mscf/STB are normalized to the same unit of measure as OOIP. However, it is difficult to assess $CO_2$ storage mass, $G_{CO2}$, across multiple $CO_2$ EOR sites. For example, while the absolute value of $CO_2$ stored in units of mass is critical to summing the total available $CO_2$ storage mass across sites (e.g., for national inventories), it is not possible to make comparisons in $CO_2$ storage resources between two reservoirs of different volume, as a larger volume allows greater storage mass. Therefore, Equation 2 can be taken one step further to express $CO_2$ storage "normalized" to OOIP, as follows:

Equation 11 provides the foundation for estimating $CO_2$ storage efficiency factors from commonly reported metrics of OOIP, R*F*, and $UF_{net}$ and plays a pivotal role in the current work.

$$\frac{G_{CO2}}{OOIP} = RF \times UF_{net\ CO2} \times \rho_{CO2} = E_{oil}\ \rho_{CO2} \qquad \text{[Eq. 11]}$$

Where $G_{CO2}/OOIP$ = specific $CO_2$ storage resource (tonnes/STB OOIP) and represents the $CO_2$ stored per unit of incremental oil volume produced through $CO_2$ EOR, and the *RF* and $UF_{net}$ terms have been combined into a single term, $E_{oil}$ (Mscf/STB OOIP).

Industry experience and simulation studies both suggest that the amount of $CO_2$ stored and, hence, the *RF* and $UF_{net}$ are a function of both geologic and operational factors. Geologic factors are specific to the reservoir and include lithology, pore type/porosity, permeability, heterogeneity, and other physical features unique to the reservoir. Operational factors are specific to the design and operation of the $CO_2$ flood, including injection pattern (the geometrical arrangement of injection and producing wells), pattern spacing (the distance between injection and producing wells), the volume of $CO_2$ injected, and the ratio of injected water to injected $CO_2$ (the WAG [water alternating gas] ratio). The interplay of geologic and operational factors leads to uncertainty in the amount of $CO_2$ storage that occurs at an individual site. Analogously, these same factors affect the quantity of incremental oil that is produced (Advanced Resources International, Inc., and Melzer Consulting, 2010; Hill and others, 2013; van't Veld and others, 2013, 2014; Ettehadtavakkol, 2014). An open research question is the degree to which these geologic and operational factors may be incorporated into approaches for $CO_2$ storage resource estimates.

The primary objective of this work was to improve $CO_2$ storage resource estimates for $CO_2$ EOR sites via integration of real-world reservoir performance data, numerical simulation studies, and statistical models to develop representative $CO_2$ storage efficiency factors for $CO_2$ EOR operations in clastic and carbonate reservoirs. The results of this work provide practical tools that can be used to quantify $CO_2$ storage resource estimates associated with $CO_2$ EOR and the uncertainty inherent in those estimates.

### Geologic Model Construction

A series of heterogeneous geologic models were created for the purpose of evaluating $CO_2$ utilization through numerical simulation of $CO_2$ enhanced oil recovery operations. Model size and shape were based on simulations of heterogeneous reservoirs performed by Gorecki and others (2009). Models were generated with an anticlinal structural trap (6.4 km [4 miles] along the anticline axis and 3.2 km [2 miles] wide). A cylindrical anticline with an arbitrary closure of 30.48 meters (100 feet) in thickness was chosen to represent the structure.

Three different model thicknesses were created: 7.6, 20, and 64 meters (25, 66, and 209 feet). Therefore, three different gridding methods were used: 1) for the 7.6-meter (25-foot)-thickness cases, the gridding was 106 × 211 × 25 with a total of 559,150 blocks; 2) for the 20-meter (66-foot)-thickness cases, the gridding was 106 × 211 × 33 with a total of 738,078 blocks; and 3) for the 64-meter (209-foot)-thickness cases, the gridding was 106 × 211 × 52 with a total 1,163,032 blocks. Geologic properties were populated within each facies using geostatistical ranges and values from the AGD (Figures 10 and 11). Porosity was assigned using a truncated normal distribution and the mean and standard deviation from the EERC AGD. The bivariate relationship between porosity and permeability was measured from porosity $\log_{10}$ (permeability) crossplots, consisting of over 1600 paired data points collected from fluvial clastic reservoirs and over 9500 pairs from carbonate shallow shelf reservoirs. These relationships were used to distribute permeability values conditioned to the previously distributed porosity properties. Petrophysical property summary statistics for each model are shown in Table 5.

Model depths of 1219 and 2438 meters (4000 and 8000 feet) were chosen to explore different temperature and pressure behaviors on the modeled system. These depths are also standards used by U.S. Energy Information Administration to calculate operating costs (U.S. Energy Information Administration, 2010). Temperature and pressure properties were based on depth properties, using a temperature gradient of 0.027°C/meter (0.015°F/foot) and a pressure gradient of 9.8 kPa/meter (0.433 psi/foot).

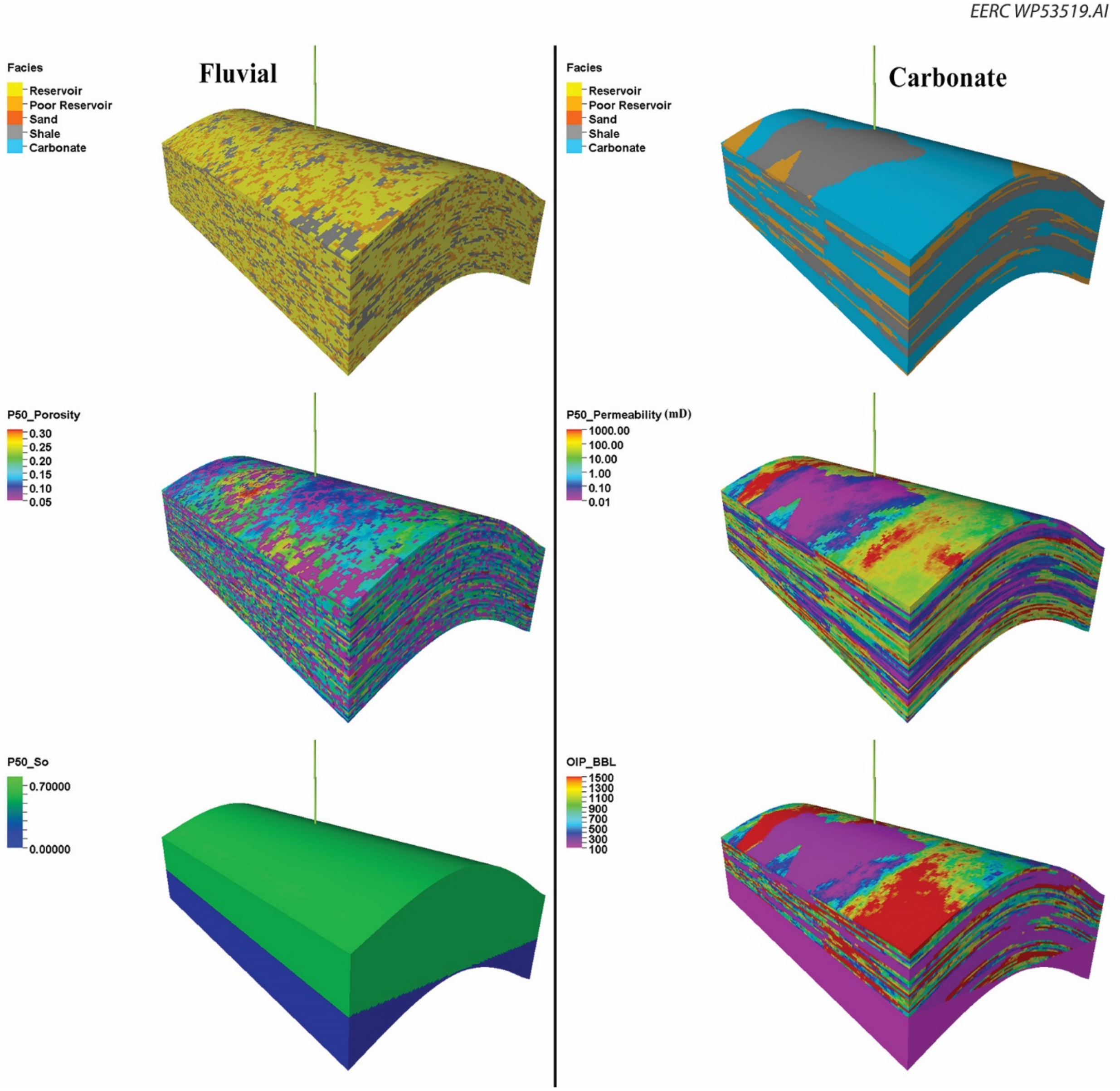

Figure 10. 64-meter (209-foot) thick anticlinal model property distributions. A single well trajectory is shown in each inset image (green vertical line). Fluvial model properties are shown in the left column, including facies, P50 porosity, and oil saturation (from top to bottom). Carbonate model properties are shown in the right column, including facies, P50 permeability (mD), and oil-in-place in barrels (from top to bottom).

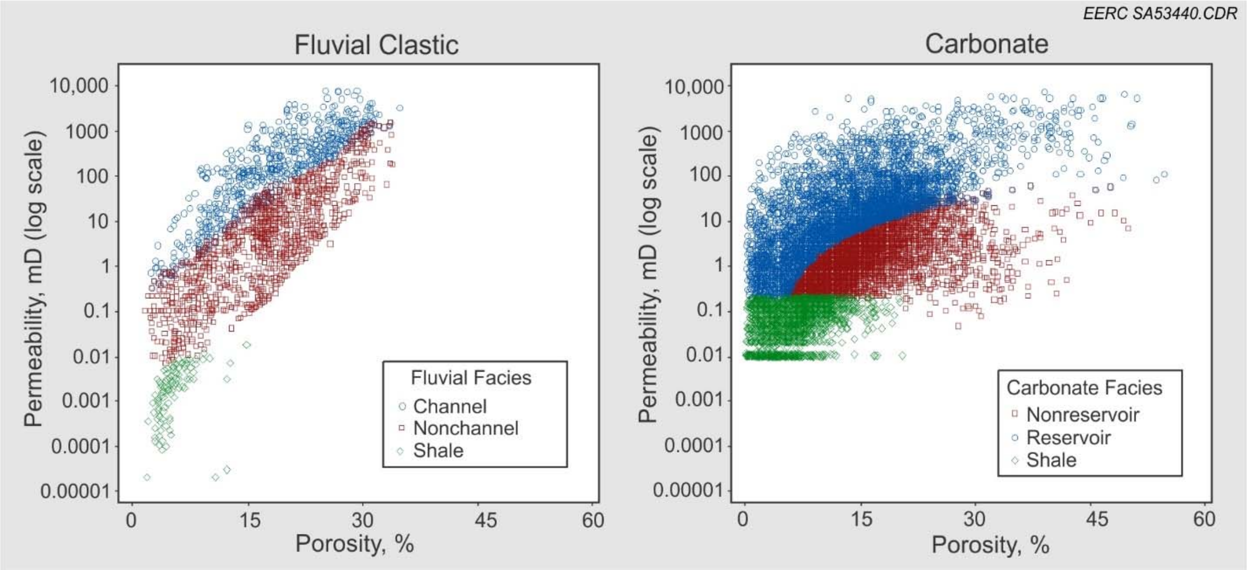

Figure 11. Porosity $\log_{10}$ (permeability) crossplots for fluvial clastic (left) and shallow shelf carbonate (right) datasets from the AGD. These porosity–permeability crossplots were used to populate the geologic properties of the simulation models for reservoir (blue circles), nonreservoir (red squares), and shale (green diamonds) lithofacies.

**Table 5. Porosity and Permeability Data Derived from the AGD for Fluvial Clastic and Shallow Shelf Carbonate Facies**

| | Fluvial Clastic | | Shallow Shelf Carbonate | |
|---|---|---|---|---|
| | **Porosity, %** | **Permeability, mD** | **Porosity, %** | **Permeability, mD** |
| Minimum | 0.31 | 0.00002 | 0.01 | 0.001 |
| P10 Mean | 5.46 | 0.05 | 3.63 | 0.08 |
| P50 Mean | 16.92 | 10.63 | 12.11 | 2.17 |
| P90 Mean | 26.62 | 670.91 | 23.00 | 76.73 |
| Maximum | 34.68 | 7983.77 | 54.42 | 7596.72 |
| Standard Deviation | 7.68 | 715.83 | 7.81 | 347.92 |

## Industry Data Set and Performance Metrics

Aside from the models constructed in these efforts, monthly reservoir performance data from 31 $CO_2$ EOR sites (hereafter referred to as the industry data set) were provided by Melzer Consulting in conjunction with a worldwide reservoir appraisal company to assist in the assessment of $CO_2$ storage in hydrocarbon reservoirs. These data were originally used to compare flood performance between differing projects, develop petroleum reserve estimates for the operators of the field, and prepare annual petroleum reserve certifications for filers with the U.S. Securities and Exchange Commission. The industry data set was described in detail in a previous publication (Azzolina and others, 2015). The data include quantity of $CO_2$ injected and produced, incremental oil recovery, and water injected for each site. The sites in the industry data set reflect WAG $CO_2$ floods – all within the continental United States and heavily dominated by the West Texas carbonate floods. Several $CO_2$ floods outside of this region were also included (i.e., the Rocky Mountain region and the state of Oklahoma).

Previous work by Azzolina and others (2015) focused on three factors that significantly influence the long-term performance and economic viability of $CO_2$ EOR projects: $CO_2$ retention, incremental oil recovery, and $CO_2$ net utilization. The current work extends the previous study by also examining $CO_2$ storage efficiency factors in accordance with Equation 11. Incremental oil recovery, $CO_2$ net utilization, and $CO_2$ storage are defined according to Equations 12–14, as shown below.

$$RF = \frac{N_p}{N} \qquad \text{[Eq. 12]}$$

Where:

$RF$ = Incremental oil recovery factor (%OOIP).
$N_p$ = Cumulative incremental oil production (STB).
$N$ = OOIP (STB).

$$UF_{net} = \frac{V_{CO2,purchased}}{N_p} \qquad \text{[Eq. 13]}$$

Where:

$UF_{net}$ = $CO_2$ net utilization factor (Mscf/STB).
$V_{CO2,purchased}$ = Cumulative volume of purchased $CO_2$ injected (Mscf).
$N_p$ = Cumulative incremental oil production (STB).

$$\mathrm{CO_2}\ \text{stored} = \mathrm{CO_2}\ \text{injected} - \mathrm{CO_2}\ \text{produced} \qquad \text{[Eq. 14]}$$

Where:

$CO_2$ stored = Volume of $CO_2$ stored (Mscf).
$CO_2$ injected = Volume of $CO_2$ injected (Mscf).
$CO_2$ produced = Volume of $CO_2$ produced (Mscf).

The volumes of $CO_2$ and water injected in the industry data set are expressed as dimensionless variables in units of hydrocarbon pore volume (HCPV), as opposed to a volume or mass measure. HCPV represents the pore volume of the reservoir that is occupied by hydrocarbons. One hundred percent HCPV (which is equivalently reported in the literature as 1.0 HCPV) is equal to the OOIP. The amount of $CO_2$ individually or $CO_2$ plus water injected is not bounded between 0 and 1.0, as more than 1.0 HCPV may be injected into the reservoir over the life cycle of the $CO_2$ flood because there is no perfect displacement, i.e., sweep efficiency, of the OOIP. We consider herein a threshold value of 3.0 HCPV as an estimate of the end of life for the $CO_2$ EOR field, recognizing that some sites may exceed this value while others may not inject up to this amount.

The input parameters required to implement Equations 12–14 to derive $CO_2$ storage efficiency factors were not available for all 31 sites in the industry data set. As a result, the focus of the measured reservoir performance data component of the current study is on nine sites from West Texas San Andres dolomite reservoirs.

### Hydrocarbon Reservoir Numerical Simulation

Numerical simulations were conducted to examine $CO_2$ storage behavior for different geologic and operational factors. The current work focused on two different $CO_2$ EOR development strategies and two different geologic regimes, with variations in reservoir volume, pressure, and temperature among these models. Two different types of $CO_2$ EOR development strategies were explored: continuous $CO_2$ injection (CCI) and WAG. In the CCI simulations, the injected fluids into the reservoir consisted solely of $CO_2$, whereas in the WAG simulations the ratio of injected water to injected $CO_2$ (WAG ratio) was 1:1. The CCI simulations represented the base case against which all other simulations are compared. There were 12 different cases for the CCI simulations. Cases 1 to 6 represent fluvial/clastic reservoirs and Cases 7 to 12 represent shallow shelf carbonate reservoirs. As discussed above, each depositional environment was simulated using two different depths (1219 and 2438 meters [4000 and 8000 feet]) and each depth was run using three different reservoir thicknesses (7.6, 20, and 64 meters [25, 66, and 209 feet]). The 50th percentile (P50 or median) outcome was generated for all 12 cases. In addition, 10th and 90th percentile (P10 and P90, respectively) outcomes were generated for a subset of four cases to assess uncertainty: Cases 2, 5, 8, and 11. Six of the 12 cases that were assessed using CCI simulation were also simulated using WAG injection. These WAG cases consisted of P50 simulations for Cases 1, 2, 6, 7, 8, and 12. Altogether, there were 18 unique simulation models (Table 6).

**Table 6. Matrix of Simulation Cases Showing the Different Lithofacies (fluvial clastic or shallow shelf carbonate), Depth (1219 or 2438 m [4000 or 8000 feet]), Thickness (7.6, 20, or 64 meters [25, 66 or 209 feet]), Temperature (48.9 or 82.2°C [120° or 180°F]), and Pressure (11.9 or 23.9 MPa [1730 or 3465 psi]).** All 12 cases generated a median (P50) outcome for CCI floods; cases marked with an "X" were also evaluated for WAG simulations.

| Case No. | Lithofacies | Depth, m/ft | Thickness, m/ft | Temp., °C/°F | Pressure, MPa/psi | WAG |
|---|---|---|---|---|---|---|
| 1 | Fluvial clastic | 1219/4000 | 7.6/25 | 48.9/120 | 11.9/1730 | X |
| 2 | Fluvial clastic | 1219/4000 | 20/66 | 48.9/120 | 11.9/1730 | X |
| 3 | Fluvial clastic | 1219/4000 | 64/209 | 48.9/120 | 11.9/1730 | |
| 4 | Fluvial clastic | 2438/8000 | 7.6/25 | 82.2/180 | 23.9/3465 | |
| 5 | Fluvial clastic | 2438/8000 | 20/66 | 82.2/180 | 23.9/3465 | |
| 6 | Fluvial clastic | 2438/8000 | 64/209 | 82.2/180 | 23.9/3465 | X |
| 7 | Shallow shelf carbonate | 1219/4000 | 7.6/25 | 48.9/120 | 11.9/1730 | X |
| 8 | Shallow shelf carbonate | 1219/4000 | 20/66 | 48.9/120 | 11.9/1730 | X |
| 9 | Shallow shelf carbonate | 1219/4000 | 64/209 | 48.9/120 | 11.9/1730 | |
| 10 | Shallow shelf carbonate | 2438/8000 | 7.6/25 | 82.2/180 | 23.9/3465 | |
| 11 | Shallow shelf carbonate | 2438/8000 | 20/66 | 82.2/180 | 23.9/3465 | |
| 12 | Shallow shelf carbonate | 2438/8000 | 64/209 | 82.2/180 | 23.9/3465 | X |

CMG-Builder was used to populate simulation model parameters and numerical settings. After setting up all the geologic properties, well placements, boundary conditions, initial conditions, fluid pressure–volume–temperature (PVT) information, rock types, and numerical parameters, the cases were sent to EERC's cluster nodes for simulation. A total of 184 CPU cores distributed in eight cluster nodes were used for the simulations.

The $CO_2$ EOR phase for the CCI simulations was run up to 3.0 HCPV. In contrast, the WAG simulations were run for over a 30-year time frame. The HCPV injected was secondary, recorded through time rather than a targeted injection volume.

Simulations were run using CMG's GEM. GEM is an advanced compositional simulator that models the flow of three-phase, multicomponent fluids. GEM has the added benefit of being able to model recovery processes where effective fluid composition is important.

Key outputs from the simulation modeling included the same metrics that were used to assess the industry data set: incremental oil recovery, $CO_2$ net utilization, and $CO_2$ storage. To permit comparisons between the simulation models and the industry data set, the simulations' injection volumes were reported in units of HCPV. All simulation modeling outputs were exported to Excel for use in the following statistical modeling and data summary.

### Statistical Modeling

A novel statistical modeling approach was used to evaluate $CO_2$ storage efficiency factors throughout the injection life cycle from 0 to 3.0 HCPV for both the industry data set and the simulation cases. The $CO_2$ storage efficiency curves during $CO_2$ EOR follow similar patterns across the industry data set and simulation cases, namely a rapid increase in storage efficiency early in the $CO_2$ flood followed by flattening, asymptotic-like behavior up to 3.0 HCPV. There are a number of nonlinear equations that describe processes that follow this pattern; however, based on previous experience in fitting these types of curves, this work explores a type of two-parameter function called Michaelis–Menten or saturation growth, which has the form (Michaelis and Menten, 1913):

$$y = \frac{ax}{(b+x)} \qquad \text{[Eq. 15]}$$

Where:

$y$ = Response variable, in this application $CO_2$ storage efficiency.
$x$ = Predictor variable, in this application cumulative $CO_2$ or $CO_2$ and water injected (HCVP).
$a$ and $b$ = Empirical constants fit using regression analysis.

One motivation for fitting an equation like Michaelis–Menten is to reduce the HCVP series data to two parameters, $a$ and $b$, about which inferences can be made. For example, in the Michaelis–Menten formula, parameter $a$ represents the maximum storage efficiency that would be possible at infinite $CO_2$ or $CO_2$ and water injection. The parameter $b$ is the time at which $CO_2$ storage efficiency is half of the maximum value. In addition to allowing inferences, the fitted model may also be used to predict the $CO_2$ storage efficiency factors out to 3.0 HCPV when the observed data, either real-world reservoir performance data or simulation data, do not reach 3.0 HCPV.

The Michaelis–Menten equation has been used to describe substrate-limited growth. In the case of $CO_2$ EOR, the substrate is the pore space available for $CO_2$ to access. The mechanistic explanation for why the Michaelis–Menten equation may be applicable to $CO_2$ EOR is as follows. During the initial $CO_2$ flood, there is sufficient available pore space for the $CO_2$ to occupy (consume) with oil or water mobilized from the same pore space. This results in the pore space "filling up" at a first-order rate, which is the period of rapid $CO_2$ storage in early time. As increasing volumes of $CO_2$ are injected, more of the accessible pore space is occupied by $CO_2$ and the available pore space decreases (gets to substrate-limited conditions), so the rate at which the pore space fills up approaches a zero-order rate. This is the period of asymptote-like or near-horizontal storage curve over time (Robert Dilmore, DOE NETL, personal communication).

The fitted Michaelis–Menten functions across sites from the industry data set and simulation cases were used to generate empirical percentile estimates of $CO_2$ storage efficiency factors.

### Results and Discussion

For the industry data set, the median times to inject 1.0, 2.0, and 3.0 HCPV of total fluids ($CO_2$ + water) were 17.3, 29.8, and 43.0 years, respectively (Table 7). The median $RF$ and $UF_{net}$ at 3.0 HCPV were 12.2% OOIP and 8.7 Mscf/STB, respectively (Table 8). Lastly, the median $E_{oil}$ at 3.0 HCPV was 1.28 Mscf/STB OOIP (Table 9).

The Michaelis–Menten model was fit to nine West Texas dolomite fields in the industry data set to generate statistical fits from 0 to 3.0 HCPV. Figure 2 shows the percentile estimates from 0 to 3.0 HCPV. The dark gray-shaded area in Figure 12 represents the interquartile range (IQR) from the 25th to 75th percentiles (P25 to P75), or the region within which 50 percent of sites are likely to fall, while the light gray-shaded area represents the P10 to P90, or the region within which 80 percent of sites are likely to fall. There is less uncertainty in the estimated $CO_2$ storage efficiency factor early in the $CO_2$ flood (small range between the P10 and P90) and greater uncertainty beyond 2.0 HCPV (larger range between the P10 and P90). For example, the P10, P50, and P90 estimates at 1.0, 2.0, and 3.0 HCPV were 0.63, 0.82, and 0.97; 0.74, 1.17, and 1.47; and 0.76, 1.28, and 1.74 Mscf/STB OOIP, respectively.

These industry data set percentiles are used to compare the results of the simulation studies. An important distinction between the industry data set results and the simulation models is that the former is specific to West Texas carbonate geology, whereas the latter is conditioned on average petrophysical relationships from the EERC AGD for either fluvial clastic or shallow shelf carbonate depositional settings and pressure/temperature conditions specific to two different reservoir depths (Table 7).

**Table 7. Summary of Time in Years Since $CO_2$ Injection as a Function of HCPV for the 12 CCI Simulation Cases, Six WAG Simulation Cases, and Median (P50) of Nine West Texas Dolomite Reservoirs from the Industry Data Set.** Blank cells mean that no data were generated in the WAG simulation cases, which were run for a time of 30 years and the volume of HCPV injected was based on the volume injected up to that point in time, not an injection target.

| | Time at HCPVI, years | | | | | |
|---|---|---|---|---|---|---|
| **Case** | **0.5** | **1.0** | **1.5** | **2.0** | **2.5** | **3.0** |
| 1 | 1.2 | 2.4 | 3.6 | 4.7 | 5.9 | 7.1 |
| 2 | 2.6 | 5.2 | 7.8 | 10.3 | 12.9 | 15.5 |
| 3 | 5.2 | 10.4 | 15.5 | 20.7 | 25.9 | 31.1 |
| 4 | 1.3 | 2.7 | 4.0 | 5.4 | 6.7 | 8.0 |
| 5 | 2.5 | 5.1 | 7.6 | 10.1 | 12.7 | 15.1 |
| 6 | 5.9 | 11.8 | 17.7 | 23.6 | 29.5 | 35.2 |
| 7 | 2.4 | 4.2 | 6.0 | 7.6 | 9.2 | 10.8 |
| 8 | 2.9 | 5.8 | 8.7 | 11.6 | 14.5 | 17.3 |
| 9 | 6.9 | 13.6 | 20.2 | 26.8 | 33.2 | 39.7 |
| 10 | 2.0 | 3.8 | 5.5 | 7.2 | 9.0 | 10.7 |
| 11 | 3.1 | 6.2 | 9.2 | 12.3 | 15.4 | 18.4 |
| 12 | 7.3 | 14.6 | 21.8 | 29.2 | 36.3 | 43.5 |
| WAG-1 | 3.5 | 6.7 | 10.0 | 13.5 | 16.8 | 20.0 |
| WAG-2 | 6.8 | 13.6 | 20.5 | 27.3 | | |
| WAG-6 | 9.1 | 18.2 | 27.4 | | | |
| WAG-7 | 6.5 | 12.3 | 17.5 | 22.7 | 27.8 | |
| WAG-8 | 8.2 | 16.4 | 24.5 | | | |
| WAG-12 | 11.0 | 22.0 | | | | |
| Industry P50 | 7.6 | 17.3 | 22.3 | 29.8 | 35.7 | 43.0 |

**Table 8. Summary of Incremental Oil Recovery in %OOIP (top) and $CO_2$ Net Utilization in Mscf/STB (bottom) as a Function of HCPV for the 12 CCI Simulation Cases, Six WAG Simulation Cases, and Median (P50) of Nine West Texas Dolomite Reservoirs from the Industry Data Set.** Blank cells mean that no data were generated.

| | **Incremental Oil Recovery Factor at HCPVI, % OOIP** | | | | | |
|---|---|---|---|---|---|---|
| **Case** | **0.5** | **1.0** | **1.5** | **2.0** | **2.5** | **3.0** |
| 1 | 3.0 | 7.0 | 9.3 | 11.0 | 12.4 | 13.5 |
| 2 | 5.1 | 11.0 | 14.5 | 16.9 | 18.7 | 20.3 |
| 3 | 5.5 | 11.0 | 14.6 | 17.2 | 19.2 | 20.8 |
| 4 | 6.8 | 10.7 | 12.7 | 14.0 | 14.9 | 15.7 |
| 5 | 9.2 | 13.8 | 16.0 | 17.4 | 18.5 | 19.2 |
| 6 | 10.2 | 15.3 | 18.1 | 20.0 | 21.3 | 22.4 |
| 7 | 4.3 | 7.3 | 9.8 | 11.8 | 13.7 | 15.3 |
| 8 | 6.2 | 11.3 | 15.2 | 18.4 | 21.0 | 23.2 |
| 9 | 5.4 | 9.2 | 12.2 | 14.5 | 16.4 | 18.1 |
| 10 | 7.1 | 12.2 | 15.9 | 18.8 | 21.2 | 23.2 |
| 11 | 9.5 | 15.2 | 18.9 | 21.6 | 23.5 | 25.0 |
| 12 | 8.7 | 13.0 | 15.7 | 17.6 | 19.1 | 20.2 |
| WAG-1 | 5.4 | 7.7 | 9.1 | 10.2 | 11.0 | 11.7 |
| WAG-2 | 6.7 | 9.7 | 11.2 | 12.3 | | |
| WAG-6 | 7.2 | 10.7 | 12.4 | | | |
| WAG-7 | 5.0 | 8.1 | 10.3 | 12.1 | 13.4 | |
| WAG-8 | 6.8 | 10.7 | 13.1 | | | |
| WAG-12 | 6.3 | 9.7 | | | | |
| Industry P50 | 2.7 | 7.3 | 10.3 | 11.7 | 12.0 | 12.2 |

| | **$CO_2$ Net Utilization at HCPVI, Mscf/STB** | | | | | |
|---|---|---|---|---|---|---|
| **Case** | **0.5** | **1.0** | **1.5** | **2.0** | **2.5** | **3.0** |
| 1 | 39.2 | 23.1 | 19.7 | 17.9 | 16.8 | 16.0 |
| 2 | 27.2 | 16.8 | 14.2 | 13.0 | 12.2 | 11.5 |
| 3 | 22.0 | 15.2 | 13.3 | 12.2 | 11.6 | 11.1 |
| 4 | 12.3 | 8.5 | 7.3 | 6.7 | 6.3 | 6.0 |
| 5 | 9.3 | 6.6 | 5.7 | 5.3 | 5.0 | 4.8 |
| 6 | 6.9 | 5.2 | 4.5 | 4.1 | 3.9 | 3.7 |
| 7 | 14.8 | 12.0 | 10.7 | 9.9 | 9.3 | 8.9 |
| 8 | 15.7 | 11.8 | 10.3 | 9.4 | 8.8 | 8.3 |
| 9 | 10.5 | 8.2 | 7.2 | 6.6 | 6.2 | 5.9 |
| 10 | 9.4 | 7.0 | 6.0 | 5.3 | 4.9 | 4.5 |
| 11 | 5.8 | 4.3 | 3.7 | 3.4 | 3.2 | 3.0 |
| 12 | 4.1 | 3.2 | 2.8 | 2.5 | 2.3 | 2.2 |
| WAG-1 | 15.1 | 12.3 | 10.9 | 10.0 | 9.4 | 8.9 |
| WAG-2 | 11.1 | 9.1 | 8.4 | 7.9 | | |
| WAG-6 | 5.2 | 4.0 | 3.5 | | | |
| WAG-7 | 9.0 | 7.1 | 6.2 | 5.7 | 5.3 | |
| WAG-8 | 8.7 | 6.7 | 5.8 | | | |
| WAG-12 | 3.2 | 2.5 | | | | |
| Industry P50 | 13.8 | 10.6 | 9.8 | 9.4 | 8.9 | 8.7 |

**Table 9. Summary of $CO_2$ Storage Efficiency ($E_{oil}$) in Mscf/STB OOIP as a Function of HCPV for the 12 CCI Simulation Cases, Six WAG Simulation Cases, and 10th Percentile (P10), 50th Percentile (median or P50), and 90th Percentile (P90) of Nine West Texas Dolomite Reservoirs from the Industry Data Set.** Yellow-shaded cells indicate where simulation data were not available and the Michaelis–Menten model fits were used to estimate $E_{oil}$ at that specific HCPV. In the Michaelis–Menten model fits, Parameter a represents $E_{oil}$ at infinite HCPV (the maximum $E_{oil}$ value) and Parameter b represents the HCPV at which the system reaches one-half of its maximum value.

| | **$E_{oil}$ at HCPVI, Mscf/STB OOIP** | | | | | | **Michaelis–Menten** | |
|---|---|---|---|---|---|---|---|---|
| **Case** | **0.5** | **1.0** | **1.5** | **2.0** | **2.5** | **3.0** | **a = $E_{oil}$ max.** | **b = HCPV at 1/2 $E_{oil}$ max.** |
| 1 | 0.83 | 1.12 | 1.27 | 1.37 | 1.44 | 1.49 | 1.80 | 0.63 |
| 2 | 0.81 | 1.08 | 1.21 | 1.28 | 1.33 | 1.37 | 1.59 | 0.49 |
| 3 | 0.73 | 1.01 | 1.16 | 1.26 | 1.33 | 1.39 | 1.70 | 0.69 |
| 4 | 0.58 | 0.63 | 0.64 | 0.64 | 0.65 | 0.65 | 0.67 | 0.08 |
| 5 | 0.50 | 0.53 | 0.54 | 0.54 | 0.53 | 0.53 | 0.55 | 0.04 |
| 6 | 0.43 | 0.48 | 0.49 | 0.50 | 0.50 | 0.50 | 0.52 | 0.10 |
| 7 | 0.44 | 0.60 | 0.72 | 0.81 | 0.88 | 0.94 | 1.31 | 1.22 |
| 8 | 0.57 | 0.78 | 0.91 | 1.00 | 1.07 | 1.13 | 1.44 | 0.85 |
| 9 | 0.34 | 0.45 | 0.53 | 0.58 | 0.61 | 0.64 | 0.79 | 0.73 |
| 10 | 0.46 | 0.59 | 0.65 | 0.69 | 0.71 | 0.72 | 0.83 | 0.40 |
| 11 | 0.32 | 0.38 | 0.41 | 0.42 | 0.43 | 0.44 | 0.47 | 0.24 |
| 12 | 0.21 | 0.25 | 0.26 | 0.26 | 0.27 | 0.27 | 0.29 | 0.16 |
| WAG-1 | 0.81 | 0.95 | 0.99 | 1.01 | 1.03 | 1.03 | 1.10 | 0.17 |
| WAG-2 | 0.74 | 0.88 | 0.94 | 0.97 | 1.00 | 1.01 | 1.09 | 0.23 |
| WAG-6 | 0.37 | 0.43 | 0.44 | 0.46 | 0.46 | 0.47 | 0.49 | 0.14 |
| WAG-7 | 0.45 | 0.58 | 0.64 | 0.68 | 0.71 | 0.72 | 0.83 | 0.42 |
| WAG-8 | 0.59 | 0.72 | 0.77 | 0.80 | 0.82 | 0.83 | 0.90 | 0.26 |
| WAG-12 | 0.20 | 0.24 | 0.25 | 0.26 | 0.26 | 0.26 | 0.28 | 0.19 |
| Industry P10 | 0.41 | 0.63 | 0.71 | 0.74 | 0.75 | 0.75 | 1.66 | 0.89 |
| Industry P50 | 0.56 | 0.82 | 1.08 | 1.17 | 1.23 | 1.28 | | |
| Industry P90 | 0.70 | 0.97 | 1.25 | 1.47 | 1.61 | 1.74 | | |

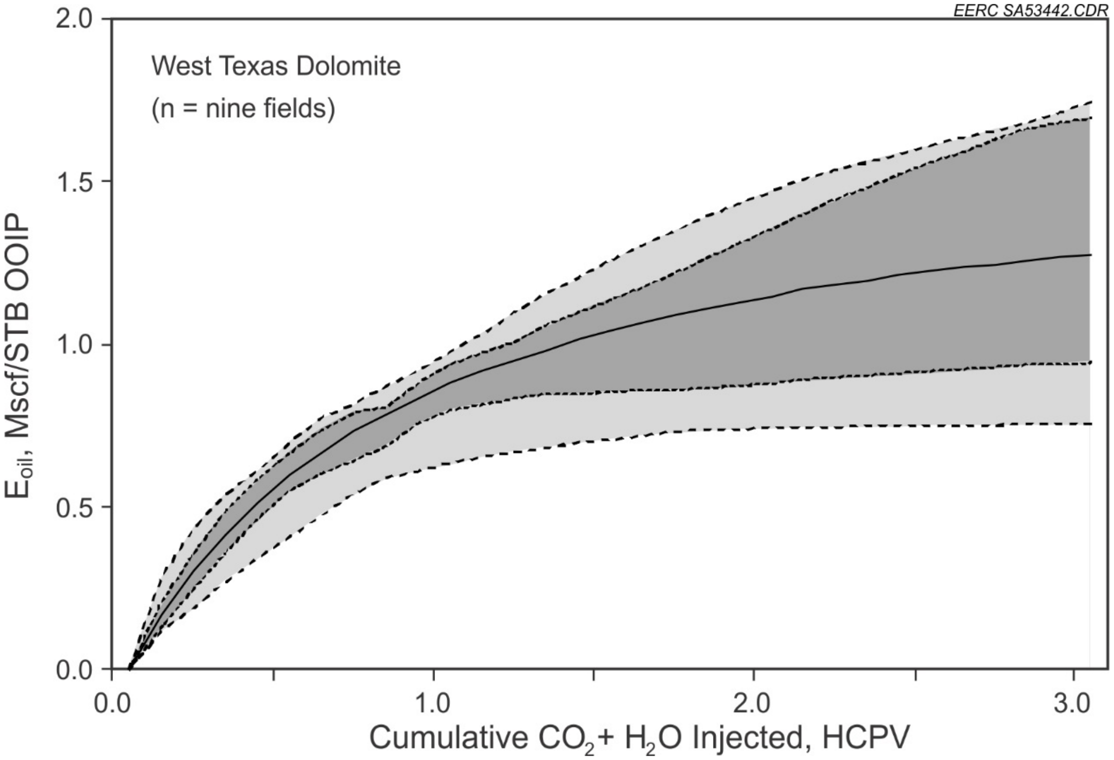

Figure 12. Percentile estimates generated from multisite Michaelis–Menten model fits for $CO_2$ storage efficiency (Mscf/STB OOIP) versus cumulative $CO_2$ + $H_2O$ injection (HCPV) for nine West Texas San Andres dolomite reservoirs. The light gray-shaded regions bounded by dashed lines represent the 10th–90th percentiles, the dark gray-shaded regions bounded by dotted lines represent the 25th–75th percentiles (interquartile range), and the P50 estimate (solid black line) represents the central value of the distribution.

### *Numerical Simulation $CO_2$ Storage Efficiency Factors*

For the CCI simulation models, the time to inject 3.0 HCPV, incremental oil recovery factor, $CO_2$ net utilization factor, and $E_{oil}$ varied as a function of lithology and reservoir thickness. The time to inject 3.0 HCPV varied from a low of 7.1 years for Case 1 (clastic, 7.6-meter [25-foot] thickness) to a maximum of 43.5 years for Case 12 (carbonate, 64-meter [209-foot] thickness) (Table 7). The incremental oil recovery factor after injection of 3.0 HCPV ranged from a low of 13.5 %OOIP for Case 1 to a high of 25.0 %OOIP for Case 11 (carbonate, 20-meter [66-foot] thickness) (Table 8). The $CO_2$ net utilization factor after injection of 3.0 HCPV ranged from a low of 2.3 Mscf/STB for Case 12 to a high of 16.8 Mscf/STB for Case 1 (Table 8). Lastly, $E_{oil}$ after injection of 3.0 HCPV ranged from a low of 0.27 Mscf/STB OOIP for Case 12 to a high of 1.49 Mscf/STB OOIP for Case 1.

The nine West Texas San Andres dolomite reservoirs in the industry data set had depth ranges from approximately 1494 to 1585 meters (4900 to 5200 feet) deep (average 1539 meters [5050 feet] deep) and thicknesses of 12 to 43 meters (40 to 140 feet) (average 27 meters [90 feet] thick), which are most similar to the physical conditions of the WAG Case 8 (1219 meters

[4000 feet] deep and 20 meters [66 feet] thick). As shown in Table 9, the simulation results after injection of 3.0 HCPV for WAG Case 8 (0.83 Mscf/STB OOIP) fell between the P10 (0.75 Mscf/STB OOIP) and the P50 (1.28 Mscf/STB OOIP) of the industry data set. Direct comparison between the simulation results and the industry data set were complicated by two characteristics. First, as mentioned above, the industry data set was specific to West Texas carbonate geology (San Andres dolomite), whereas the simulation results were conditioned on average petrophysical relationships from the EERC AGD for shallow shelf carbonate depositional settings and pressure/temperature conditions specific to reservoir depths of 1219 and 2438 meters (4000 and 8000 feet). Second, the industry data set represented a synopsis of historical operations for fields that operated since the early 1980s. The evolution of these fields, including the impact of infill drilling or changes to the $CO_2$ flood plan over time, are not explicitly quantified by the statistical analyses provided in Azzolina and others (2015).

### *Dimensionless $CO_2$ Storage Efficiency Factors*

The statistical population of the geologic models using the average petrophysical relationships from the EERC's AGD resulted in slightly different reservoir effective pore volumes across Cases 1–12. These differences confound drawing inferences about $E_{oil}$ that are attributable to differences in reservoir depth (1219 and 2438 meters [4000 and 8000 feet]), thickness (7.6, 20, or 64 meters [25, 66, or 209 feet]), lithology (clastic or carbonate), or $CO_2$ flood development strategy (CCI versus WAG). Moreover, work on DSFs expresses $CO_2$ storage efficiency in dimensionless units, which are not directly comparable to the units shown in Table 9. Therefore, Table 10 expresses dimensionless $E_{oil}$ values for the simulation cases using the following calculation approach. For the reservoir simulation models used in Cases 1–12, the total volume of $CO_2$ stored and the reservoir effective pore volume were known explicitly. Therefore, the $CO_2$ storage efficiency can be expressed as the ratio of these values, which is the dimensionless $E_{oil}$ value:

$$E_{oil}(\text{dimensionless}) = \frac{V_{CO2}}{V_{\phi eff}} \qquad \text{[Eq. 16]}$$

Where:

$V_{CO2}$ = reservoir volume of $CO_2$ stored
$V_{\phi eff}$ = effective pore volume of the reservoir

Figure 13 shows the dimensionless $CO_2$ storage efficiency curves from simulation model outputs for both the fluvial clastic and shallow shelf carbonate simulations and their associated Michaelis–Menten model fits.

Figure 13 illustrates several interesting trends about the relative differences in $CO_2$ storage efficiency across the different model cases. First, comparing clastic and carbonate models shows that for all but Cases 4 and 10 (left-most panel in the middle row), the clastic models have greater $CO_2$ storage efficiency than the carbonate models under the same reservoir thickness and depth conditions (i.e., the solid black lines are above the solid blue lines in the different panels in Figure 13). These results are a by-product of the porosity–permeability distributions for clastic versus carbonate reservoirs – for a given porosity, the clastic models have greater permeability because of the greater slope of the porosity–permeability bivariate relationship (Figure 11). In

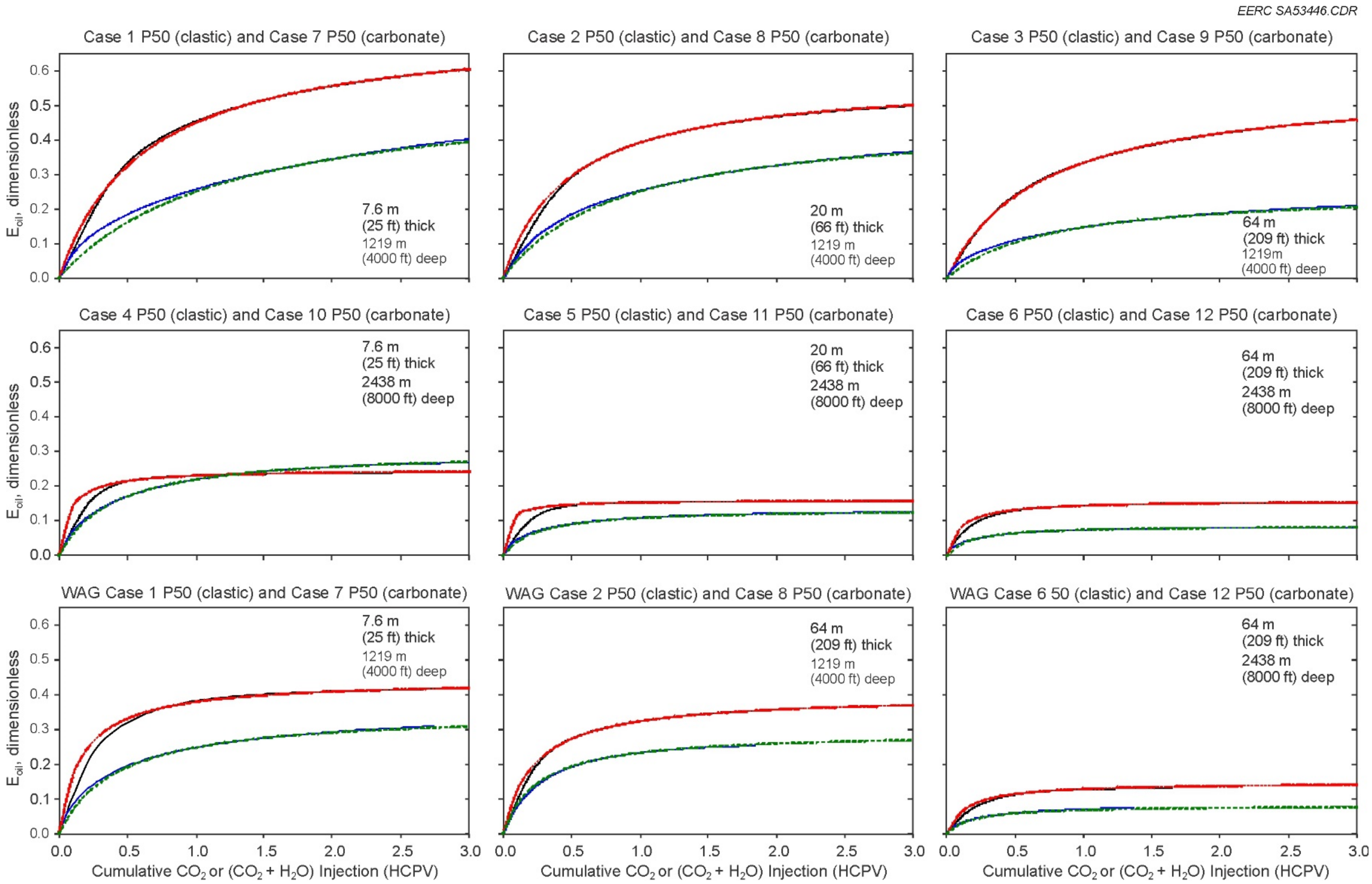

Figure 13. Cumulative $CO_2$ or ($CO_2$ + $H_2O$) injected (HCPV) versus $CO_2$ storage efficiency ($E_{oil}$, dimensionless units) for the fluvial clastic (black solid lines) and shallow shelf carbonate (blue solid lines) simulation models. The solid lines show the simulation model output and the dashed lines represents the fitted Michaelis–Menten model. The top six panels represent the CCI simulations and the bottom three panels represent WAG simulations. While the former were run to 3.0 HCPV, the latter were run for 30 years of injection and the HCPV injected was based on the amount injected over that period.

addition, comparing CCI simulations to WAG simulations shows that the CCI development yields a higher $CO_2$ storage efficiency. For example, the dimensionless $E_{oil}$ values after injection of 3.0 HCPV for CCI clastic Cases 1, 2, and 6 are 61%, 50%, and 15%, respectively. In contrast, the dimensionless $E_{oil}$ values after injection of 3.0 HCPV for WAG clastic Cases 1, 2, and 6 are 42% (31% less), 37% (26% less), and 14% (7% less), respectively (Table 10). These trends are also true for carbonate models. The dimensionless $E_{oil}$ values after injection of 3.0 HCPV for CCI carbonate Cases 7, 8, and 12 are 40%, 37%, and 8%, respectively. In contrast, the dimensionless $E_{oil}$ values after injection of 3.0 HCPV for WAG carbonate Cases 7, 8, and 12 are 31% (23% less), 21% (27% less), and 8% (no change), respectively. The greater $CO_2$ storage efficiency under the CCI development strategy is attributable to the fact that during WAG injection, water occupies pore space that might otherwise store $CO_2$, hence WAG development results in lower $E_{oil}$. This is also reflected in the lower $CO_2$ net utilization rates for the WAG cases, which were approximately 20% to 45% less than their CCI counterparts at a given HCPV of total fluids injected (Table 8). Lastly, the dimensionless $E_{oil}$ values at a particular HCPV are greater in the 1219-meter (4000-foot) reservoirs (top row in Figure 3) than in the 2438-meter (8000-foot) reservoirs (middle row in Figure 13), which illustrates a dependency of $E_{oil}$ on reservoir pressure and temperature conditions.

**Table 10. Summary of $CO_2$ Storage Efficiency ($E_{oil}$) in Dimensionless Units ($V_{CO2}/V\Phi eff$) as a Function of HCPV for the 12 CCI Simulation Cases and Six WAG Simulation Cases.** Yellow-shaded cells indicate where simulation data were not available and the Michaelis–Menten model fits were used to estimate $E_{oil}$ at that specific HCPV. In the Michaelis–Menten model fits, parameter a represents $E_{oil}$ at infinite HCPV (the maximum $E_{oil}$ value) and parameter b represents the HCPV at which the system reaches one-half of its maximum value.

| | **$E_{oil}$ at HCPVI, %** | | | | | | **Michaelis–Menten** | |
|---|---|---|---|---|---|---|---|---|
| **Case** | **0.5** | **1.0** | **1.5** | **2.0** | **2.5** | **3.0** | **a = $E_{oil}$ max.** | **b = HCPV at 1/2 $E_{oil}$ max.** |
| 1 | 33 | 46 | 52 | 55 | 58 | 61 | 73 | 0.63 |
| 2 | 29 | 39 | 44 | 47 | 49 | 50 | 58 | 0.49 |
| 3 | 24 | 33 | 38 | 42 | 44 | 46 | 56 | 0.69 |
| 4 | 22 | 23 | 24 | 24 | 24 | 24 | 25 | 0.08 |
| 5 | 15 | 16 | 16 | 16 | 16 | 16 | 16 | 0.04 |
| 6 | 13 | 15 | 15 | 15 | 15 | 15 | 16 | 0.10 |
| 7 | 19 | 26 | 31 | 35 | 38 | 40 | 56 | 1.22 |
| 8 | 19 | 25 | 30 | 33 | 35 | 37 | 47 | 0.85 |
| 9 | 11 | 15 | 17 | 19 | 20 | 21 | 26 | 0.73 |
| 10 | 17 | 22 | 24 | 26 | 27 | 27 | 31 | 0.40 |
| 11 | 9 | 11 | 12 | 12 | 12 | 13 | 14 | 0.24 |
| 12 | 6 | 7 | 8 | 8 | 8 | 8 | 8 | 0.16 |
| WAG-1 | 33 | 38 | 40 | 41 | 42 | 42 | 45 | 0.17 |
| WAG-2 | 27 | 32 | 34 | 36 | 36 | 37 | 40 | 0.23 |
| WAG-6 | 11 | 13 | 13 | 14 | 14 | 14 | 15 | 0.14 |
| WAG-7 | 19 | 25 | 27 | 29 | 30 | 31 | 35 | 0.42 |
| WAG-8 | 19 | 23 | 25 | 26 | 27 | 27 | 29 | 0.26 |
| WAG-12 | 6 | 7 | 7 | 8 | 8 | 8 | 8 | 0.19 |

Figure 13 also shows that the Michaelis–Menten model accurately describes the overall shape of the $CO_2$ storage efficiency curves for both the fluvial clastic and shallow shelf carbonate simulations. For the deeper clastic models (Cases 4, 5, and 6), which quickly reach their asymptote at approximately 0.5 HCPV, the Michaelis–Menten model overpredicts $E_{oil}$ in the region between 0 and 0.5 HCPV. Nevertheless, the Michaelis–Menten model provides a simple and effective tool for modeling $E_{oil}$ as a function of HCPV using a single analytical expression.

In aggregate, Figure 13 illustrates relationships between $E_{oil}$ and lithofacies, reservoir thickness, reservoir depth (a surrogate for reservoir pressure and temperature), and $CO_2$ flood development (CCI or WAG). As seen in Figure 13, the $CO_2$ storage efficiency factors are more strongly influenced by depth and reservoir geology than by reservoir volume (thickness). Thus in terms of screening-level assessments for estimating the $CO_2$ storage resource in $CO_2$ EOR operations, reservoir depth (or pressure and temperature) and lithology may play a more significant role in estimating the $CO_2$ storage efficiency factor than reservoir volume.

Figure 14 shows contour plots of dimensionless $E_{oil}$ for the CCI cases for clastic and carbonate reservoirs as a function of reservoir depth (*y*-axis) and thickness (*x*-axis). Figure 14, therefore, provides a response surface for dimensionless $E_{oil}$ as a function of lithology, depth, and thickness. These plots not only illustrate the differences between clastic and carbonate, but also allow predictions of $E_{oil}$ at future $CO_2$ EOR sites. For example, a carbonate reservoir 1829 meters (6000 feet) deep and 30.5 meters (100 feet) thick would be expected to yield and $E_{oil}$ of approximately 20%, while the same conditions for a clastic reservoir would be expected to yield an $E_{oil}$ of approximately 0.3.

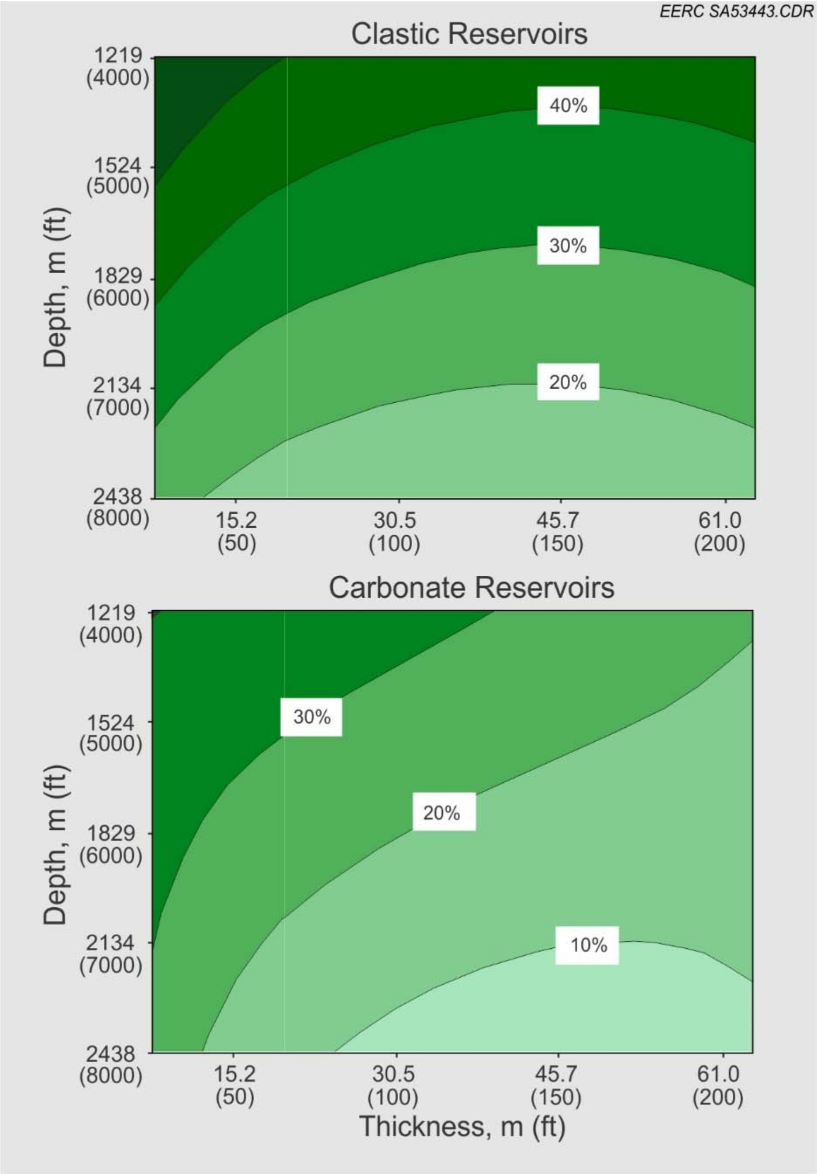

Figure 14. Contour plots of simulated $E_{oil}$ for the CCI cases for fluvial clastic reservoirs (top) and shallow shelf carbonate reservoirs (bottom) as a function of reservoir depth (y-axis) and thickness (x-axis).

### *Comparison to $E_{saline}$ Estimates*

Several studies have focused on DOE methodology and $CO_2$ storage efficiency factors for deep saline reservoirs, or $E_{saline}$. These works provide $E_{saline}$ for displacement terms when $E_{An/At}$ (ratio of net to total area), $E_{hn/hg}$ (ratio of net to gross thickness), and $E_{\phi e/\phi tot}$ (ratio of effective to total porosity) values are known directly, which are the conditions of simulation Cases 1–12. Literature P10 and P90 estimates of $E_{saline}$ for clastic, limestone, and dolomite reservoirs are 7.4 to 24%, 10 to 21%, and 16 to 26%, respectively (Goodman and others, 2011; U.S. Department of Energy National Energy Technology Laboratory, 2012). As shown in Table 10, dimensionless $E_{oil}$

at 3.0 HCPV for the CCI development strategies in clastic and carbonate reservoirs ranged from 46 to 61% and 21 to 40% for the 1219-meter (4000-foot) reservoirs and 12 to 24% and 8 to 27% for the 2438-meter (8000-foot) reservoirs, respectively. Thus, the dimensionless $E_{oil}$ values in this study can be considerably higher than previous estimates of $E_{saline}$, depending on reservoir conditions and $CO_2$ development strategy. A primary reason for the greater $E_{oil}$ values is that these $CO_2$ EOR fields are not only injecting $CO_2$, but are also producing fluids ($CO_2$, oil, and water) at the production wells. Therefore, the addition of fluid extraction creates additional pore space into which the $CO_2$ can be permanently stored, thus increasing the overall $CO_2$ storage efficiency.

## CONCLUSIONS

The results of the DSF assessment described in this report provide general values and distributions for $CO_2$ storage efficiency in closed and semiclosed hydrogeologic systems from eight different models representing ten depositional environments. Closed- and semiclosed boundary conditions were employed over a 100-year injection time frame to develop results relevant to future potential commercial-scale CCS operations using an array of injection wells. The regional-scale extent of the models constructed in these efforts were simulated as a unit cell within a formation-scale assessment, surrounded on all sides by other unit cells. The pressure interference between unit cells caused wells to experience closed or semiclosed boundary conditions.

Storage efficiency values for 1219-meter (4000-foot) depths ranged from 0.29% for carbonate shelf to 0.58% for carbonate peritidal depositional environments, while storage efficiency values for 2438-meter (8000-foot) depths ranged from 0.56% for carbonate shelf to 1.32% for carbonate peritidal depositional environments. The narrow range in $E_{saline}$ values across models, attributable to the closed or semiclosed system boundary conditions of the simulations, did not distinguish significant differences among depositional environments at the end of 100 years of $CO_2$ injection. This suggests that the effect of depositional environment on $CO_2$ storage efficiency is negligible in a closed system. However, the results illustrate the relative importance of depositional environment, formation depth, structural geometry, and boundary conditions on the *rate* of $CO_2$ storage in closed or semiclosed systems. The type of depositional environment responsible for generating a particular formation results in different degrees of lateral and vertical heterogeneity and ranges in petrophysical property characteristics, which together affect $CO_2$ injection rate by controlling fluid flow and pressure dispersion.

The modeling and simulation showed the relative influence of reservoir depth, structure, and boundary conditions on $CO_2$ storage efficiency. Reservoir depth plays an important role in controlling $CO_2$ injection rate by constraining the amount of force (pressure) which may be used during injection. The maximum injection pressure constraint (gradient) was 13.6 kPa/m (0.6 psi/ft); therefore, the deeper models permitted greater $CO_2$ injection rates over the 100-year period. Geologic structure exerts a similar influence on $CO_2$ storage efficiency, as shown in this study by the greater $CO_2$ storage efficiency in anticline models as compared to flat (structureless) models. The depth difference between the hinge and limbs of the anticline structures used in the current study was approximately 152.4 meters (500 feet), which resulted in greater $\Delta p$ (change between initial and final reservoir pressure) along the deeper limbs of the anticline allowing a greater amount of $CO_2$ to be injected. Boundary conditions exert the greatest control on $CO_2$ injection rate by allowing or resisting pressure dispersion. In open systems, which are confined vertically but open laterally, pore space (and thus pressure dissipation) for the injected $CO_2$ is created primarily by lateral displacement of formation water. Conversely, a closed system does not permit mass transfer across either vertical or lateral boundaries, and space for the injected $CO_2$ is solely attributable to in situ fluid compressibility and pore dilation (the inverse of compressibility). The closed-boundary systems modeled in this work showed lower $CO_2$ storage efficiency values than prior work conducted on open systems. These closed-boundary estimates may be more representative of $CO_2$ storage resource potential in commercial-scale fields using an array of injection wells over 100-year time frames.

The fluvio-deltaic and clastic shelf environments of the DSF investigation exhibited the greatest $CO_2$ storage rates among the environments considered in this study. This was largely due to a high frequency of desirable petrophysical characteristics contained within the EERC AGD. This suggests that these types of deposits may be of primary interest to future investigations of prospective storage resource and may serve to assist in $CO_2$ storage complex screening. However, variability occurs within each depositional environment. Similar depositional processes may result in different ratios of reservoir and poor-reservoir/nonreservoir rock and different ranges of petrophysical characteristics. Location-specific data plays a key role in reducing uncertainty in $CO_2$ storage resource assessment and should be given careful consideration in the movement toward successful commercial-scale CCS.

The results of the hydrocarbon reservoir assessment provide useful statistical information to estimate $CO_2$ storage efficiency in $CO_2$ EOR operations. $CO_2$ storage efficiency values derived from real-world reservoir performance data from the industry data set, all of which were WAG $CO_2$ floods, resulted in P10, P50, and P90 estimates for $CO_2$ storage efficiency factors in West Texas San Andres dolomite reservoirs of 0.76, 1.28, and 1.74 Mscf/STB OOIP. Across fluvial clastic and shallow shelf carbonate simulation models, median $CO_2$ storage efficiency factors from CCI following conventional waterflood varied from 0.50 to 1.49 and 0.27 to 1.13 Mscf/STB OOIP, respectively. Median $CO_2$ storage efficiency factors from WAG $CO_2$ injection varied from 0.47 to 1.03 and 0.26 to 0.83 Mscf/STB OOIP for fluvial clastic and shallow shelf carbonate reservoirs, respectively, demonstrating that WAG injection results in lower $CO_2$ storage efficiency than CCI.

When expressed on a dimensionless scale, median $CO_2$ storage efficiency factors from CCI following conventional waterflood varied from 15% to 61% and 8% to 40% for fluvial clastic and shallow shelf carbonate simulation models, respectively. Median $CO_2$ storage efficiency factors from WAG $CO_2$ injection varied from 14% to 42% and 8% to 31% for fluvial clastic and shallow shelf carbonate reservoirs, respectively. These storage efficiency values are considerably higher than previous estimates of efficiency values for DSFs. This is primarily attributable to $CO_2$ EOR fields both injecting $CO_2$ and simultaneously producing fluids ($CO_2$, oil, and water) at the production wells. Therefore, the addition of fluid extraction creates additional pore space into which the $CO_2$ can be permanently stored, thus increasing the overall $CO_2$ storage efficiency. Variation in the $CO_2$ storage efficiency factors was largely attributable to reservoir depth (a surrogate for reservoir pressure and temperature) and lithology (clastic versus carbonate lithofacies).

For sites currently undergoing $CO_2$ injection with total fluid injection volumes above 1.0 HCPV, it may be possible to estimate the incremental oil recovery factor and $CO_2$ net utilization separately and then apply the methods described in Azzolina and others (2015) to estimate $CO_2$ storage. However, if there are no site-specific values available, then the $CO_2$ storage efficiency values presented in this work may be used to estimate $CO_2$ storage based solely on the reservoir OOIP.

The research activities for both the DSFs and conventional hydrocarbon reservoirs associated with $CO_2$ EOR supported the development of a best practices manual on optimizing and quantifying $CO_2$ storage resources in these geologic settings. Using lessons learned from this work and other DOE-funded research, approaches outlined in the best practices manual present workflows that guide the user through a series of decision points that help determine which $CO_2$ storage resource-estimating method is best for a particular situation. The methodologies for the optimization and refinement of $CO_2$ storage resource estimation that are presented in the best practices manual will enable stakeholders to more accurately estimate the $CO_2$ storage resource potential in these geologic formations.

## REFERENCES

Advanced Resources International, Inc., and Melzer Consulting, 2010, Optimization of $CO_2$ storage in $CO_2$ enhanced oil recovery projects: Department of Energy & Climate Change (DECC) Office of Carbon Capture & Storage, November 30.

Azzolina, N.A., Nakles, D.V., Gorecki, C.D., Peck, W.D., Ayash, S.C., Melzer, L.S., and Chatterjee, S., 2015, $CO_2$ storage associated with $CO_2$ enhanced oil recovery—a statistical analysis of historical operations: International Journal of Greenhouse Gas Control, v. 37, p. 384–397.

Bachu, S., 2015, Review of $CO_2$ storage efficiency in deep saline aquifers: International Journal of Greenhouse Gas Control, v. 40, September, p. 188–202.

Bachu, S., Bonijoly, D., Bradshaw, J., Burruss, R., Holloway, S., Christensen, N.P., and Mathiassen, O.M., 2007, International Journal of Greenhouse Gas Control, v. 1, no. 4, p. 430–443.

Bear, J., 1972, Dynamics of fluids in porous media: New York, Elsevier.

Birkholzer, J.T., and Zhou, Q., 2009, Basin-scale hydrogeologic impacts of $CO_2$ storage—capacity and regulatory implications: International Journal of Greenhouse Gas Control, published online on 8/8/2009, DOI: 10.1016/j.ijggc.2009.07.002.

Birkholzer, J.T., Zhou, Q., and Tsang, C.F., 2009, Large-scale impact of $CO_2$ storage in deep saline aquifers—a sensitivity study on pressure response in stratified systems: International Journal of Greenhouse Gas Control, v. 3, p. 181–194.

Boggs, S., 2001, Principles of sedimentology and stratigraphy (3d ed.): Upper Saddle River, New Jersey, Prentice Hall.

Brady, C.L., and Lee, S.K., 1998, A comparison of forecast and actual production after a decade of field operations in the alpha unit polymer-augmented waterflood: Presented at the 1998 Society of Petroleum Engineers/U.S. Department of Energy Improved Oil Recovery Symposium held in Tulsa, Oklahoma, April 19–22, Paper SPE-39614.

Calhoun Jr., J.C., 1982, Fundamentals of reservoir engineering: Norman, Oklahoma, University of Oklahoma Press.

Canadian Standards Association, 2012, CSA Group Z741-12 geologic storage of carbon dioxide: Mississauga, Ontario, Canada, October.

Cavanagh, A.J., and Wildgust, N., 2011. Pressurization and brine displacement issues for deep saline formation $CO_2$ storage: Energy Procedia, v. 4, p. 4814–4821, DOI:10.1016/j.egypro.2011.02.447.

Devore, J.L., 2004, Probability and statistics for engineering and the sciences (6th ed.): Belmont, California, Brooks/Cole Publishing.

Esken, A., Höller, S., Vallentin, D., and Viebahn, P., 2012, CCS global—prospects of carbon capture and storage technologies (CCS) in emerging economies: Final technical report, Part III: Country study China, report, 214 p.

Ettehadtavakkol, A., Lake, L.W., and Bryant, S.L., 2014, $CO_2$-EOR and storage design optimization: International Journal of Greenhouse Gas Control, v. 25, p. 79–92.

Fitch, P.J.R., Lovell, M.A., Davies, S.J., Pritchard, T., and Harvey, P.K., 2015, An integrated and quantitative approach to petrophysical heterogeneity: Marine and Petroleum Geology, v. 63, p. 82–96.

Gao, P., Sorensen, J., Braunberger, J., Doll, T., Smith, S., Gorecki, C., Hawthorne, S., Steadman, E., and Harju, J., 2014, Updated regional technology implementation plan for Zama: Plains $CO_2$ Reduction (PCOR) Partnership Phase III, Task 15 – Deliverable D86.

Gibling, M.R., 2006, Width and thickness of fluvial channel bodies and valley fills in the geological record—a literature compilation and classification: Journal of Sedimentary Research, v. 76, p. 731–770.

Goodman, A., Bromhal, G., Strazisar, B., Rodosta, T., Guthrie, W.F., Allen, D., and Guthrie, G., 2013, Comparison of methods for geologic storage of carbon dioxide in saline formations: International Journal of Greenhouse Gas Control, v. 18, p. 329–342.

Goodman, A., Hakala, A., Bromhal, G., Deel, D., Rodosta, T., Frailey, S., Small, M., Allen, D., Romanova, V., Fazio, J., Huerta, N., McIntyre, D., Kutchko, B., and Guthrie, G., 2011, U.S.

DOE methodology for the development of geologic storage potential for carbon dioxide at the national and regional scale: International Journal of Greenhouse Gas Control, v. 5, p. 952–965.

Gorecki, C.D., Sorensen, J.A., Bremer, J.M., Ayash, S.C., Knudsen, D.J., Holubnyak, Y.I., Smith, S.A., Steadman, E.N., and Harju, J.A., 2009, Development of storage coefficients for carbon dioxide storage in deep saline formation: Report for U.S. Department of Energy Cooperative Agreement, Grand Forks, North Dakota, Energy & Environmental Research Center, 61 p.

Henninges, J., Liebscher, A., Bannach, A., Brandt, W., Hurter, S., Köhler, S., and Möller, F., CO2SINK Group, 2011, P-T-p and two-phase fluid conditions with inverted density profile in observation wells at the $CO_2$ storage site at Ketzin (Germany): Energy Procedia, no. 4, p. 6085–6090.

Henson, R., Todd, A., and Corbett, P., 2002, Geologically based screening criteria for improved oil recovery projects: SPE/DOE Improved Oil Recovery Symposium, Tulsa, Oklahoma, April, SPE 75148.

Hill, B., Hovorka, S., and Melzer, S., 2013, Geologic carbon storage through enhanced oil recovery: Energy Procedia, v. 37, p. 6808–6830.

IEA Greenhouse Gas R&D Programme, 2014, $CO_2$ storage efficiency in deep saline formations—a comparison of volumetric and dynamic storage resource estimation methods: 2014-09, October.

IEA Greenhouse Gas R&D Programme, 2009, Development of storage coefficients for $CO_2$ storage in deep saline formations: 2009/12, October.

IEA Greenhouse Gas R&D Programme, 2012, Extraction of formation water from $CO_2$ storage: Technical report to U.S. Department of Energy and IEA Greenhouse Gas R&D Programme, 2012/12.

Kolterman, C.E., and Gorelick, S.M., 1996, Heterogeneity in sedimentary deposits—a review of structure-imitating, process-imitating, and descriptive approaches: Water Resources Research, v. 32, no. 9, p. 2617–2658.

Koottungal, L., 2014, 2014 worldwide EOR survey: Oil and Gas Journal special report, http://www.ogj.com/articles/print/volume-112/issue-4/special-report-eor-heavy-oil-survey/2014-worldwide-eor-survey.html (accessed June 2017).

Kuuskraa, W., and Wallace, M., 2014, $CO_2$-EOR sets for growth as new $CO_2$ supplies emerge: Oil and Gas Journal, v. 112, no. 4, p. 66–77.

Lake, L.W., 1989, Enhanced oil recovery: Englewood Cliffs, New Jersey, Prentice Hall.

Leach, A., Mason, C.F., and van't Veld, K., 2011, Co-optimization of enhanced oil recovery and carbon sequestration: Resource & Energy Economics, v. 33, no. 4, p. 893–912.

Liu, D., and Li, W., 2013, Flue gas enhanced oil recovery (EOR) as a high efficient development technology for offshore heavy oil in China: Journal of Petroleum and Gas Engineering, v. 4, no. 5, p. 127–142, doi:10.5897/JPGE2013.0155.

Melzer, L.S., 2012, Carbon dioxide enhanced oil recovery ($CO_2$ EOR)—factors involved in adding carbon capture, utilization and storage (CCUS) to enhanced oil recovery. Midland Texas: Report for the National Enhanced Oil Recovery Initiative, http://neori.org/Melzer_CO2EOR_CCUS_Feb2012.pdf (accessed June 2017).

Michaelis, L., and Menten, M.L., 1913, The kinetics of invertase action: Biochemistry Z, v. 49, p. 333–369.

Newman, G., 1973, Pore volume compressibility of consolidated, friable, and unconsolidated reservoir rocks under hydrostatic loading: SPE Journal of Petroleum Technology, v. 25, p. 129–134.

Peck, W.D., Glazewski, K.A., Klenner, R.C.L., Gorecki, C.D., Steadman, E.N., and Harju, J.A., 2014, A workflow to determine $CO_2$ storage potential in deep saline formations: Energy Procedia, v. 63, p. 5231–5238.

Peck, W.D., Gorecki, C.D., Steadman, E.N., and Harju, J.A., 2015, Optimizing and quantifying $CO_2$ storage resource in saline formations and hydrocarbon reservoirs: Task 3 interim report.

Peridas, G., 2008, Spinning straw into black gold—enhanced oil recovery using carbon dioxide: Written testimony submitted to the U.S. House of Representatives Natural Resources Committee Subcommittee on Energy and Mineral Resources hearing, June 12.

Steadman, E.N., Sorensen, J.A., Gorecki, C.D., Hamling, J.A., Liu, G., Klapperich, R.J., Bailey, T.P., Bremer, J.M., Braunberger, J.R., Smith, S.A., Botnen, L.A., Holubnyak, Y.I., Schmidt, D.D., and Harju, J.A., 2010, The Basin Electric Power Cooperative carbon capture and storage project—a geological characterization report detailing key elements and paths forward for two injection scenarios: Technical report.

Thibeau, S., and Mucha, V., 2011, Have we overestimated saline aquifer $CO_2$ storage capacities? Oil & Gas Science and Technology-Rev. IFP Energies Nouvelles, v. 66, no. 1, p. 81–92, DOI: 10.2516/ogst/2011004.

U.S. Department of Energy National Energy Technology Laboratory, 2010, Carbon dioxide enhanced oil recovery—untapped domestic energy supply and long term carbon storage solution: Strategic Center for Natural Gas and Oil, March.

U.S. Department of Energy National Energy Technology Laboratory, 2007, The carbon sequestration atlas of the United States and Canada: Office of Fossil Energy.

U.S. Department of Energy National Energy Technology Laboratory, 2012, The 2012 United States carbon utilization and storage atlas (4th ed.) (Atlas IV).

U.S. Department of Energy National Energy Technology Laboratory, 2015, The 2015 United States carbon utilization and storage atlas (5th ed.) (Atlas IV).

U.S. Energy Information Administration, 2010, Oil and gas lease equipment and operating costs 1994 through 2009: p. 1–8.

Van't Veld, K., Mason, C.F., and Leach, A., 2013, The economics of $CO_2$ sequestration through enhanced oil recovery: Energy Procedia, v. 37, p. 6909–6919.

Van't Veld, K., Wang, X., and Alvarado, V., 2014, Economic co-optimization of oil recovery and $CO_2$ sequestration: Presented at the Society of Petroleum Engineers Annual Technical Conference and Exhibition, Amsterdam, The Netherlands, October 27–29, SPE–170880-MS.

Zhang, H., Wen, D., Li, Y., Zhang, J., and Lu, J. 2005. Conditions for $CO_2$ geological sequestration in China and some suggestions: Geological Bulletin of China, v. 24, no. 12, p. 1107–1110, DOI: CNKI:SUN:ZQYD.0.2005-12-004.

Zhou, Q., Birkholzer, J.T., Tsang, C.-F., Rutqvist, J., 2008, A method for quick assessment of $CO_2$ storage capacity in closed and semi-closed saline formations: International Journal of Greenhouse Gas Control, v. 2, no. 4, p. 626–639.